Accepted to Ap. J.
Preprint typeset using LaTeX style emulateapj v. 8/13/10

arXiv:1104.2619v2 [astro-ph.CO] 18 Apr 2011

OBSCURED GOODS AGN AND THEIR HOST GALAXIES AT $Z < 1.25$: THE SLOW BLACK HOLE GROWTH PHASE

B. D. Simmons[1,2], J. Van Duyne[3], C. M. Urry[1,2], E. Treister[4,5,7], A. M. Koekemoer[6], N. A. Grogin[6] and the GOODS team
1 Astronomy Department, Yale University, New Haven, CT 06511, USA
2 Yale Center For Astronomy & Astrophysics, Physics Department, Yale University, New Haven, CT 06511, USA
3 Northrup Grumman, 5500 Canoga Ave, Woodland Hills, CA 91364, USA
4 Institute for Astronomy, 2680 Woodlawn Drive, University of Hawaii, Honolulu, HI 96822, USA
5 Universidad de Concepción, Departamento de Astronomìa, Casilla 160-C, Concepción, Chile and
6 Space Telescope Science Institute, 3700 San Martin Drive, Baltimore, MD 21218, USA
Accepted to Ap. J.

ABSTRACT

We compute black hole masses and bolometric luminosities for 87 obscured AGN in the redshift range $0.25 \leq z \leq 1.25$, selected from the GOODS deep multi-wavelength survey fields via their X-ray emission. We fit the optical images and obtain morphological parameters for the host galaxy, separating the galaxy from its central point source, thereby obtaining a four-band optical SED for each active nucleus. We calculate bolometric luminosities for these AGN by reddening a normalized mean SED of GOODS broad-line AGN to match the observed central point-source SED of each obscured AGN. This estimate of L_{bol} has a smaller spread than simple bolometric corrections to the X-ray luminosity or direct integration of the observed multi-wavelength SED, suggesting it is a better measure. We estimate central black hole masses from the bulge luminosities. The black hole masses span a wide range, $7 \times 10^6 M_\odot$ to $6 \times 10^9 M_\odot$; the median black hole mass is $5 \times 10^8 M_\odot$. The majority of these AGN have $L/L_{Edd} \leq 0.01$, and we detect no significant evolution of the mean Eddington ratio to $z = 1.25$. This implies that the bulk of black hole growth in these obscured AGN must have occurred at $z \gtrsim 1$ and that we are observing these AGN in a slow- or no-growth state.

Subject headings: galaxies: active — galaxies: nuclei — galaxies: fundamental parameters — galaxies: bulges — galaxies: Seyfert — methods: data analysis

1. INTRODUCTION

Accurately estimating the mass and growth of supermassive black holes (SMBHs) in the centers of massive galaxies is critical to the field of galaxy formation and evolution. Calculations of black hole masses from direct observables have been limited to only a few methods: stellar kinematics from within the black hole sphere of influence (Genzel et al. 1997; Ghez et al. 2005); H_2O maser kinematics (Miyoshi et al. 1995; Herrnstein et al. 1999; Greenhill et al. 2003); kinematics of central gaseous disks (Ford et al. 1994; Ferrarese & Ford 1999); and reverberation mapping (Peterson 1993; Peterson & Wandel 2000). These methods, while powerful and tested, are mostly restricted to bright galaxies and luminous active galactic nuclei (AGN) in the local universe.

Far more common are obscured AGN, which by definition have a reddened (fainter) central point source and often resemble a normal galaxy at optical and near-infrared wavelengths. These comprise a large fraction of all AGN and contribute much of the X-ray background (Ueda et al. 2003; Treister & Urry 2005, 2006; Treister et al. 2004, 2006, 2008, 2009). The high luminosity ratio between host galaxy and obscured point source makes indirect black hole mass ($M_\bullet$) estimates, such as the $M_\bullet - L$ (where L is the galaxy or bulge luminosity) relation (Marconi & Hunt 2003), much more promising than in quasar hosts, as well as one of the only methods available given that nuclear emission, including broad lines, is usually obscured in these sources.

Combining black hole masses with bolometric luminosities gives an important intrinsic property of AGN, the Eddington ratio, $\lambda \equiv L/L_{Edd}$, as well as the associated dimensionless accretion rate, $\dot{m}_{acc} \equiv \dot{M}c^2/L_{Edd}$. These quantities indicate how fast a black hole is growing: only accretion approaching (or exceeding) the Eddington limit leads to an appreciable increase in black hole mass. From well-studied spectral energy distributions (SEDs) of unobscured Type 1 quasars (Sanders et al. 1988; Elvis et al. 1994; Richards et al. 2006), one can derive bolometric corrections for AGN with less complete SEDs (Elvis et al. 1994; Fabian & Iwasawa 1999; Elvis et al. 2002; Marconi et al. 2004; Hopkins et al. 2007). However, these bright quasars are rare among the larger AGN population (AGN found in deep *Chandra* exposures are generally $10 - 100$ times less luminous) and bolometric corrections for the more common, lower-luminosity AGN are much less certain.

Detailed study of large samples of AGN and host galaxies has recently become possible via large multi-wavelength surveys (e.g., GOODS, COSMOS, ECDFS) that include X-ray and infrared data as well as high-resolution, deep optical imaging with the Hubble Space Telescope (*HST*). The unparalleled resolution of the Advanced Camera for Surveys (ACS) resolves typical AGN host galaxies and point sources out to $z \sim 1$ (Sánchez et al. 2004; Ballo et al. 2007; Pierce et al. 2007; Alonso-Herrero et al. 2008; Gabor et al. 2009, but

brooke.simmons@yale.edu
[7] *Chandra* Fellow.

also see, *e.g.,* Grogin et al. 2003 and Schawinski et al. 2011 for other *HST* instruments), and simulations have confirmed the reliability of host and point-source separation for obscured AGN out to these redshifts (Simmons & Urry 2008). Here, we utilize the Great Observatories Origins Deep Survey (GOODS, Giavalisco et al. 2004) X-ray through 24 μm data to characterize separately the active nuclei and the host galaxies of a large sample of moderate luminosity, obscured AGN.

The separation of the host galaxy from the AGN point source allows us to determine simultaneously the SED of the AGN alone and the $M_\bullet$ (from the host galaxy, using the $M_\bullet$-L_B relation, where L_B is the rest-frame B-band bulge luminosity). We can then extrapolate the AGN luminosity to the far-infrared based on the level of reddening in the optical point source, and thus estimate the bolometric luminosity. Coupled with black hole mass, this allows us to determine Eddington luminosities and ratios for obscured AGN over the redshift range of $0.25 < z < 1.25$. We discuss the data and sample selection in Section 2. Section 3 describes the black hole mass estimation, including treatment of time variability of the black hole-bulge luminosity relation, and Section 4 details how we calculate bolometric luminosities and discusses the reliability of our methods. In Section 5 we discuss the derived Eddington luminosities and ratios for our sample.

Throughout this paper, we adopt $H_0 = 71$ km/s/Mpc, $\Omega_M = 0.27, \Lambda_0 = 0.73$, consistent with the *WMAP* cosmology (Spergel et al. 2003).

2. DATA

2.1. *Sample Selection*

In order to reliably extract AGN light from the combined light of an AGN plus its host galaxy, we require deep observations using an instrument with a point-spread function (PSF) that is small compared to the size of the galaxy. The excellent depth and resolution of the of the GOODS *HST* observations provide an excellent opportunity for studying moderate-luminosity AGN ($L_X = 10^{42} - 10^{44}$erg s^{-1}) out to high redshifts ($z \geq 2$). The GOODS data include the space-based Chandra Deep Fields in the X-ray (0.5-8 keV; Giacconi et al. 2002; Alexander et al. 2003), four *HST*/ACS filters in the optical (F435W, B; F606W, V; F775W, i; F850LP, z_{850}; Giavalisco et al. 2004), all four *Spitzer*/IRAC bands in the infrared (3.6, 4.5, 5.8, 8.4 μm), *Spitzer*/MIPS 24 μm (Treister et al. 2006, Dickinson et al., in preparation, Chary et al., in preparation) and the ground-based FLAMINGOS J and K bands and SOFI/ISAAC JHK bands for GOODS-North and South, respectively.

We define our AGN sample by the following criteria:

1. *Chandra* X-ray point source matched to an optically-detected source using a maximum-likelihood method to more than 99% confidence (Bauer et al. 2004).

2. Spectroscopic redshifts (Cowie et al. 2003; Wirth et al. 2004; Szokoly et al. 2004) at $z \leq 1.25$, so that the data cover the rest-frame B-band.

3. Total absorption-corrected hard X-ray luminosity, L_X (2-8 keV) $\geq 3 \times 10^{42}$erg s^{-1} to minimize contamination from pure starburst galaxies with no AGN (Persic et al. 2004).

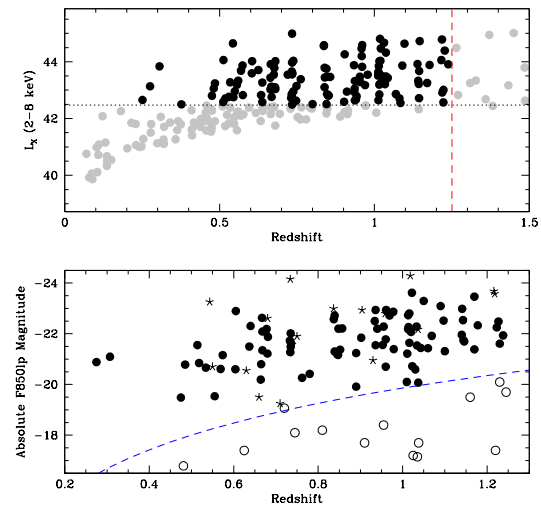

FIG. 1.— *Top:* Hard X-ray luminosity vs. redshift for GOODS X-ray-selected, optical z_{850}-detected galaxies with spectroscopic redshifts. The AGN sample defined by our X-ray and redshift selection criteria (dashed lines; $L_X > 3 \times 10^{42}$ erg s^{-1}, $z < 1.25$) are black; excluded sources are gray. *Bottom:* Absolute z_{850} host magnitude vs. redshift for the sample AGN in the top panel. For accurate morphological fitting, we also require sources with host $z_{850} < 24$ mag (blue dashed line) and a stellarity index indicative of an extended source (< 0.85). All 87 sources meeting those criteria are shown as black filled circles. Faint sources with host $z_{850} > 24$ are shown as open circles; point-like sources with host $z_{850} < 24$ are shown as stars.

This results in an initial sample of 121 AGN, with 68 from GOODS-North and 53 from GOODS-South. We apply further criteria to select a sub-sample of sources with high enough *HST* data quality for two-dimensional host galaxy fitting.

To separate a source's central (optical) AGN light from its host galaxy light using two-dimensional parametric fitting techniques requires high-resolution data and relatively high signal-to-noise for each source (> 5 per pixel). To ensure the highest quality fits, we include only sources with host $z_{850} \leq 24$ mag (AB), and with a stellarity parameter (estimated by the SExtractor parameter, `CLASS_STAR`; Bertin & Arnouts 1996) less than 0.85, where `CLASS_STAR` = 1 is a pure point source. Following this cut, we retain 90 AGN (51 from GOODS-N, 39 from GOODS-S), of which 9 are broad-line objects. Figure 1 shows the distributions of L_X, M_{850lp}, and z for X-ray sources with $z < 1.25$ in the GOODS fields. We further exclude three sources for which we were unable to isolate the bulge flux. Two have extremely irregular and disrupted optical morphology, making morphological descriptions in terms of bulges and disks meaningless, and one has a marginal `CLASS_STAR` = 0.845; all three are among the lowest optical luminosity, with a mean $M_B = -19.05$, nearly an order of magnitude below the next lowest AGN host ($M_B = -20.2$; see Figure 1). The remaining 87 AGN+hosts constitute our final sample.

2.2. *Point Source-Host Galaxy Decomposition*

We perform morphological decomposition of the GOODS AGN+host galaxies using the 2-D fitting rou-

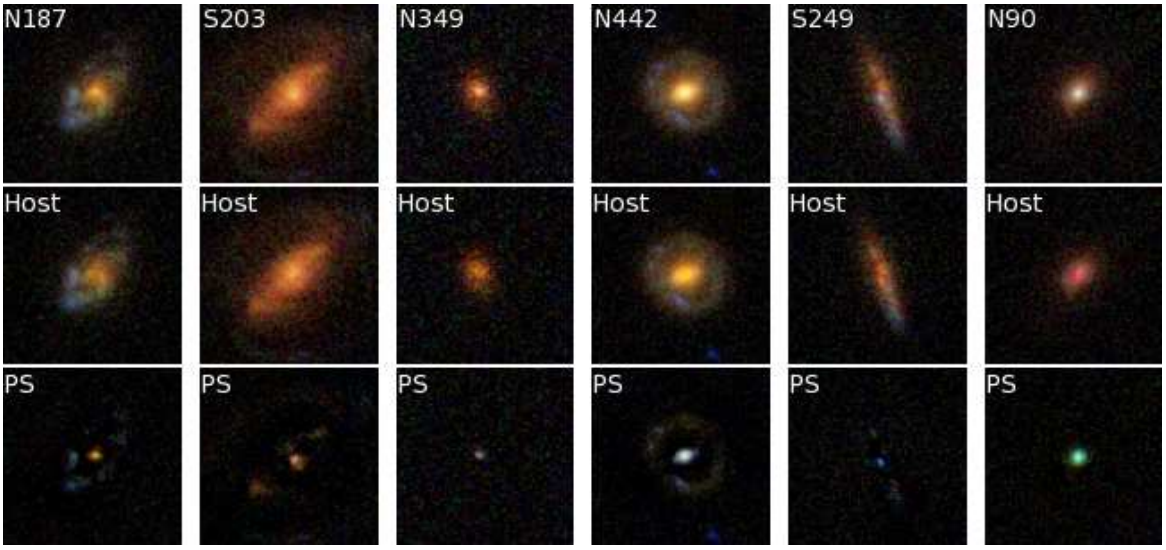

FIG. 2.— $BVIz$ composite images of six of the sources in our sample. Each source, marked with its ID from Alexander et al. (2003), is fit in each band with a host galaxy composed of a bulge and disk, and a central point-source. For each source, the image marked "Host" shows the point-source-subtracted galaxy. The image marked "PS" shows the residuals when the smooth host galaxy fit is subtracted, leaving behind the central nucleus and extended detailed features of the host galaxy. Hosts and point sources vary in color and luminosity. (SEDs of these sources are shown in Figure 5.)

tine GALFIT (Peng et al. 2002). This routine allows for simultaneous fitting of one or more host galaxy components along with a central point source. We used the GOODS ACS images that were processed using the STScI Multidrizzle algorithm (Koekemoer et al. 2002), improving the native resolution to 0.03 arcsec/pixel.

We fit each source independently in each ACS band (B, V, I, and z_{850}) with a three-component fit: a deVaucouleur bulge + an exponential disk + a nuclear point source, the latter of which is modeled by a noiseless, analytical PSF based on analysis of dozens of real stars in the GOODS fields, created independently for each band using the IRAF package daophot. This PSF creation method minimizes the effects of potential eccentricities of any one star on the field (such as color or excess noise), while still accounting for any possible deviations within our drizzled data from a purely analytical PSF created from a package such as TINY TIM (Krist 1993).

Each galaxy was initially fit using an automated program (described in further detail in Simmons & Urry 2008, hereafter S08) that uses SExtractor catalog values as initial parameter guesses. The primary goal of the initial fit is to fix the central positions of the host and point source and to calculate initial estimates of the fit parameters. Each galaxy was then fit with GALFIT by hand to achieve the best possible fit, assessed using the χ^2 goodness-of-fit parameter and examination of fit residuals. We then calculate the rest-frame B-band bulge-to-total ratios and point-source and host galaxy luminosities, using the InterRest interpolation code from Taylor et al. (2009); see Table 1 for total, point source, and host galaxy magnitudes and associated errors. Separated hosts and point sources for six objects in our sample are shown in Figure 2.

Reliable calculations of AGN black hole mass and bolometric luminosity require accurate measurements of each source's host galaxy-to-point source luminosity and bulge-to-total ratios, which are determined by our morphological fitting. S08 simulated over 50,000 AGN host galaxies in order to assess the limits of the morphological fitting. The simulations show that the determination of L_{host}/L_{PS} is generally reliable to the flux and redshift limits of our sample. Brighter point sources introduce greater uncertainty into the recovered parameters, especially the host galaxy magnitude and bulge-to-disk ratio (S08). We add these uncertainties in quadrature with the fit errors, which in turn affects the uncertainties in our black hole masses and Eddington ratios.

For samples like ours, automated fitting of AGN and hosts recovers at least 90% of central point sources (S08); our recovery fraction should be higher due to the fact that we fit each source individually. S08 also find a spurious point-source detection rate of approximately 12% in a single-band sample with equal numbers of bulge- and disk-dominated sources. However, this is an upper limit for our sample, since the chance of spurious detections or unrecovered point sources in multiple bands for a single source is extremely small. Statistically, the probability of a missed point source in 2 (3, 4) bands is 1% (0.1%, 0.01%) for one source. The probability of a spurious detection in 2 (3, 4) bands for a source with equal contributions from a bulge and disk is 1.4% (0.2%, 0.02%), though this calculation varies with the morphology of each source. Based on the number of point sources detected in our sample and each source's individual morphology (following S08), we expect that we miss $\lesssim 3$ point source detections within the sample and have spurious detections for ~ 2 sources.

Rest-frame B-band properties of each host galaxy and central point source are given in Table 1.

3. BLACK HOLE MASS ESTIMATION

Direct kinematic measurements of black hole mass are not possible for the majority of our sample because most of the AGN are obscured. Instead we use black hole-bulge relations to estimate the black hole masses. We use the point-source-subtracted bulge luminosity to calculate $M_\bullet$ from rest-frame B-band absolute magnitudes of the host galaxy bulge using the $M_\bullet - L_B$ relation from

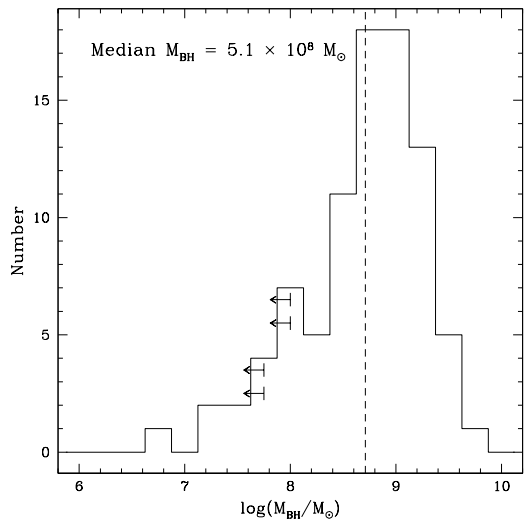

FIG. 3.— Histogram of estimated black hole masses, using bulge luminosities from morphological fitting and Equation 1, adapted from Marconi & Hunt (2003). The dashed line shows the median value of $M_\bullet = 5.1 \times 10^8 M_\odot$. Arrows indicate the four sources with upper limits to the black hole mass.

Eq. 19 of Ferrarese & Ford (2005) as converted from Marconi & Hunt (2003):

$$\log(\mathrm{M}_\bullet) = (8.37\pm0.11)-(0.419\pm0.085)(\mathrm{B_B}+20.0), \quad (1)$$

where B_B is the rest-frame B-band absolute magnitude of the galaxy bulge. Rest-frame B bulge-only absolute magnitudes range from $-16.32 > B_B > -23.27$, with an average error of $\sigma_B = 0.13$ (determined from `GALFIT` uncertainties added in quadrature to systematic uncertainties from S08). Within our sample, we find bulge fractions ranging from $< 5\%$ to 100%, with a median bulge-to-total ratio of 0.54. For the four cases where a bulge is undetected in the rest-frame B, we follow S08 in assuming a maximum of 5% bulge contribution, and consider those black hole masses upper limits.

The mass-luminosity relation of Eq. 1 is based on measurements in the local universe. Treu et al. (2004) have shown an evolution in the relation out to redshift $z = 0.3$: the rest-frame B-band mass-to-light ratio of the bulge decreases with redshift due to the fact that a higher-redshift bulge typically has a younger stellar population than a bulge at $z = 0$. Subsequent work on different samples and using different methods (Borys et al. 2005; Alexander et al. 2008; Bluck et al. 2011) finds that black hole masses seem to lag behind bulges at even higher redshift, implying that black hole masses calculated from bulge properties are overestimated by approximately a factor of 3 at $z \sim 1$.

However, several other studies (Woo et al. 2005; Peng et al. 2006; Woo et al. 2008; Jahnke et al. 2009; Decarli et al. 2010; Merloni et al. 2010) report a decrease in the intrinsic bulge stellar mass-black hole mass relation with redshift, in the sense that bulge mass appears to evolve faster than black hole mass within our redshift range, leading to an evolution in the bulge-black hole mass relation in the opposite direction. Some of the conflicting results may be explained by differences resulting from comparing black hole masses to different quantities (stellar mass versus bulge luminosity, for example), but the picture is not yet clear. Black hole masses calculated at $z \sim 1$ may change by a factor of approximately 3 in either direction and still be consistent with previous studies.

Going forward, we quote the unevolved masses, calculated via a Monte Carlo method in order to account for uncertainties in host luminosity and bulge-to-total ratio (both determined from S08) as well as the intrinsic scatter noted in Equation 1 and an additional uncertainty of ±0.47 dex to encompass the uncertainty in the evolution of Eq. 1 to the redshifts relevant to our sample. We generate 10^5 data points for each of our 87 sources, with uncertainties folded into each step to calculate black hole masses; the reported $M_\bullet$ values and errors represent the peak and σ values of the Monte Carlo distribution for each object. This method typically results in SMBH mass uncertainties of approximately ±0.5 dex in log-$M_\bullet$. Using the same Monte Carlo method, we propagate these errors through to our calculation of Eddington ratios (discussed in Section 5).

The resulting black hole masses are shown in Figure 3 and presented in Table 1. The majority (94%) are between $5.0\times10^7 < M_\bullet < 5.5\times10^9$ $\mathrm{M}_\odot$, and the rest have masses (or upper limits) down to $M_\bullet = 6.7 \times 10^6$ $\mathrm{M}_\odot$. The median mass, $M_\bullet = 5.1 \pm 4.7 \times 10^8$ $\mathrm{M}_\odot$, is indicated on Figure 3 as a dashed line.

4. BOLOMETRIC LUMINOSITY CALCULATIONS

In order to study the properties of AGN, we need to know the total power they emit. Bolometric luminosities of AGN are thus important quantities, but they are also difficult to calculate directly for many populations of AGN. Owing to our selection criteria, the SEDs of our 87 sources are typically dominated by galaxy light at optical and near-IR wavelengths, so we do not expect that naively summing the luminosities of our sources at all wavelengths will provide a reliable estimate of total AGN power.

We therefore consider two alternative approaches: (1) an average bolometric correction to the X-ray luminosity based on unobscured broad-line AGN (§ 4.1), and (2) individual corrections based on fitted reddening of our main AGN sample (§ 4.2).

4.1. *X-ray Bolometric Correction*

Bolometric luminosities are commonly estimated using an X-ray bolometric correction, K_X, where $L_{bol,X} = K_X L_X$. Values of K_X have been derived from well-defined SEDs of optically selected, powerful quasars and range from $K_X \sim 10$ (Elvis et al. 1994) to $K_X \approx 33$ (Fabian & Iwasawa 1999) or $K_X > 50$ (Elvis et al. 2002). The K factor is luminosity- and wavelength-dependent (Marconi et al. 2004; La Franca et al. 2005; Treister & Urry 2005).

The bulk of our sample lies more than an order of magnitude below the average L_X of mean quasar SEDs such as those computed from the Sloan Digital Sky Survey (Richards et al. 2006). This suggests the K_X values from the literature may not accurately represent our sample. Since the GOODS data cover nearly 5 decades of wavelength, we calculate our own K_X value and compare to previously derived K_X.

First, we develop an SED for unobscured, broad-line AGN by averaging the 58 GOODS sources with clear

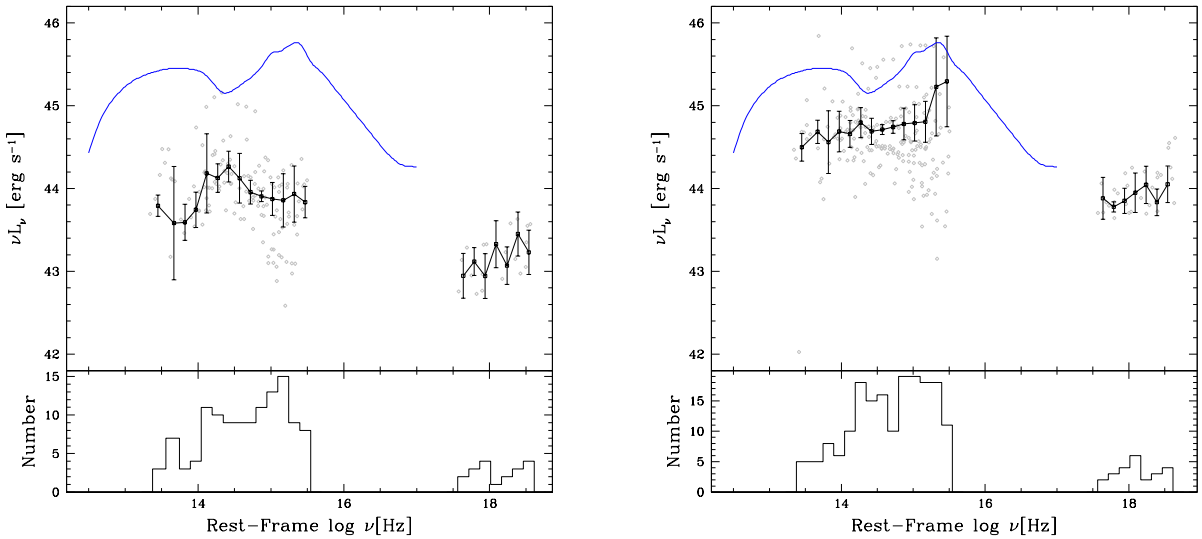

FIG. 4.— Weighted average SEDs of broad-line AGN in the GOODS fields (filled circles). The left panel shows 32 low-luminosity ($43.0 < \log L_X < 44.0$) AGN, and the right panel shows 26 moderate-luminosity ($44.0 < \log L_X < 44.9$) AGN. The bottom histogram in each panel shows the number of AGN contributing to the median, as a function of frequency. For comparison, the average spectrum of more luminous SDSS quasars ($L_X > 10^{45}$ erg s^{-1}; Richards et al. 2006) is shown as a blue dashed line. Our SEDs are very roughly consistent with the Richards et al. spectrum when normalized at ~ 1 keV, but the "big blue bump" feature at $\sim 2500\AA$ is significantly weaker in lower luminosity AGN. Note that some lower-luminosity objects used to make the composite SED in the left panel show signs of a K-giant stellar population in their SEDs.

broad lines and hence low reddening (Barger et al. 2003; Szokoly et al. 2004; Cowie et al. 2004), as well as $N_H < 10^{21}$ cm^{-2} (Bauer et al. 2004). We also impose the criterion $L_X > 10^{43}$ erg s^{-1} to minimize host galaxy contamination in the optical and near-IR. (Three of these sources are in our sample of 87 AGN.) Even under these conditions, 12 of the selected broad-line AGN show some signs of a K-giant stellar population in their SEDs (Barger et al. 2003; Mainieri et al. 2005), particularly at lower L_X. We then split the unobscured sample into two groups, less than and greater than $L_X = 10^{44}$ erg s^{-1}, to investigate the dependency of K_X on L_X. The median, absorption-corrected, 2-8 keV X-ray luminosity for each group is 2.4×10^{43} and 1.4×10^{44} erg s^{-1}, respectively, consisting of 32 and 26 AGN, respectively.

Figure 4 shows the rest-frame, error-weighted geometric mean of our intermediate-luminosity AGN in frequency bins 0.15 dex in width. Given the wide redshift range, not all wavelength bins include the same number of photometric bands for each unique object. In addition to weighting by photometric error in each bin, we also weight by the fraction of AGN in each band with respect to the total sample number (shown in the bottom panel of Figure 4).

For comparison, we also plot in Figure 4 the mean SDSS quasar SED from Richards et al. (2006). The "big blue bump" in both GOODS AGN samples (at $\sim 2500\AA$) is considerably weaker than in SDSS quasars, relative to the mean luminosity at 1 μm. This suggests that using an SDSS-derived K_X estimate would overestimate the bolometric luminosity in our AGN sample.

The integrated luminosities of the averaged broad-line AGN source SEDs are calculated by summing the 2-30 keV rest-frame L_X, the 1250 Å-8 μm broad-band luminosities and the integrated UV-to-soft X-ray assuming $L_\nu \propto \nu^{1.41}$. This results in integrated luminosities and bolometric corrections of $L_{bol,BL}(8\ \mu\text{m} - 30\text{keV}) = 4.1 \times 10^{44}$ erg s^{-1} and $K_X = 14.4^{+18.6}_{-7.7}$ for the lower-luminosity broad-line AGN, and $L_{bol,BL}(8\ \mu\text{m} - 30\text{keV}) = 2.6 \times 10^{45}$ erg s^{-1} and $K_X = 15.2^{+16.5}_{-7.4}$ for the higher-luminosity broad-line AGN. The K_X value in the lower-luminosity broad-line AGN may be slightly high due to host contamination of the optical and near-infrared SED (we estimate this contamination increases K_X in the lower luminosity sample by $\approx 20\%$).

4.2. *Point-Source Reddening / Dust Luminosity Method*

We can derive the observed point-source SED in the four ACS bands using the results from morphological fitting. In some sources, typically in the ACS B (and possibly V) bands of higher-redshift sources, no point source is detected at all; in these cases, we calculate an upper limit for these bands based on the residual background flux. Figure 5 shows six examples of total broad-band SEDs (diamonds) from 24 μm to U-band, plus X-ray, and the point-source optical SEDs as red squares.

We redden an unobscured AGN template to fit the extracted point source luminosities. We use the two averaged AGN SEDs calculated in the previous section, choosing which template to use for each source based on the source's X-ray luminosity. First, we normalize the template to the absorption-corrected, hard X-ray luminosity of each source. After this normalization, the mean SED exceeds the observed rest-frame broad-band MIR luminosity by more than the uncertainty of the mean SED for only eight of our 87 sources. This indicates that the choice of template SEDs is appropriate for our sample.[2] In the rare case where the SED exceeds the

[2] If we were to instead use the Richards et al. (2006) SDSS quasar template, the template would exceed the MIR flux in 68% of sources.

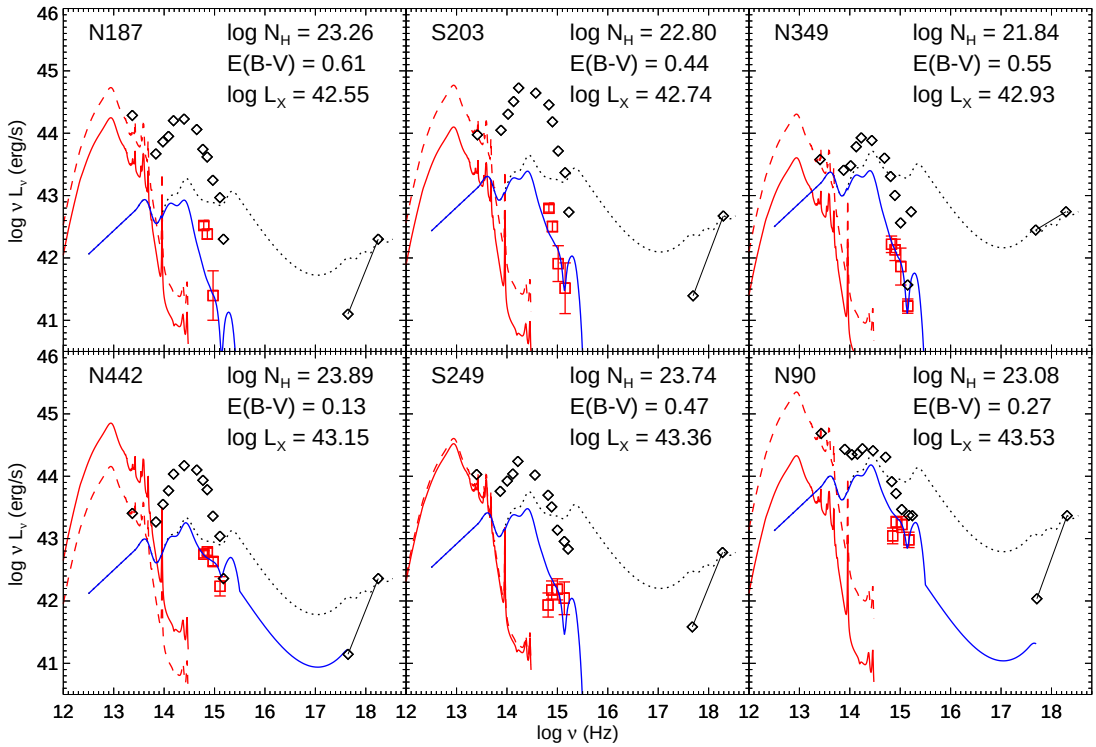

FIG. 5.— Broad-band SEDs of AGN plus host galaxy (*open diamonds*) and point source alone (*red squares*). The mean AGN SED, calculated from broad-line AGN within the GOODS fields, is shown as a *dotted line*, normalized to the AGN hard X-ray luminosity. This template was reddened and fit through the extracted point source values, resulting in the *blue solid curve*. The far-IR dust curve (*solid red line*) is calculated from the derived $E(B-V)$ according to Draine & Li (2007). Shown for comparison is the same emissivity normalized to the maximum L_{MIR} from broad-band flux (*dashed red line*). In most cases, the calculated (solid) curve lies under the maximum (dashed) curve, *i.e.,* the calculated infrared luminosities do not exceed the observed luminosities. In the rare event that the solid line exceeds the observed infrared flux (N442), it is usually by a small factor ($\times 2$), commensurate with AGN variability on year-long timescales (Sarajedini et al. 2006). (Images of these sources are shown in Figure 2.)

observed MIR luminosity after normalizing to the hard X-ray luminosity, the mean SED is re-normalized to be consistent with the observed MIR luminosity.

We then fit the normalized spectrum to the optical point-source SED, applying the reddening curve of Cardelli et al. (1989) for a Milky Way ISM ($R_V = 3.1$) over the wavelength range of $0.1 < \lambda < 3.5$ μm and using a χ^2-minimization algorithm to calculate the reddening value of the nuclear emission. For sources with point source detections in three or four filters ($N_{pt} \geq 3$), the reddening average is $\langle E(B-V)\rangle = 0.47 \pm 0.37$. This increases to $\langle E(B-V)\rangle = 0.78 \pm 0.54$ for AGN with solid detections in only two bands. We note that point source SEDs with significantly different colors from the host galaxy SED are frequent enough in our sample that attempting to determine the reddening value from the combined AGN+host SED would be considerably less reliable. This is consistent with previous simulations and observations (*e.g.*, Pierce et al. 2010a,b).

The independent determination of $E(B-V)$ from reddening and N_H from X-ray absorption allows us to estimate the dust-to-gas ratio along the line of sight (Section 4.4). We can then estimate the total re-radiated IR luminosity of the material that is absorbing optical and UV photons from the point source, using the dust emissivity models of Draine & Li (2007) and the dust-to-gas ratios to convert the emissivity profiles to luminosity, L_{dust}.

This calculation requires two assumptions: (1) the ambient radiation field strength, U, near the dust, and (2) the physical line-of-sight path length, l, through the AGN and host galaxy. We select the Draine & Li (2007) model that has a range of $U = (1 - 1 \times 10^5)U_0$, where $U = \int_{0.09}^{8\ \mu\mathrm{m}} 4\pi J_\lambda = 4.34 \times 10^{-2}$ erg cm^{-2} s^{-1} (Mathis et al. 1983), to roughly reproduce the combination of AGN radiation field strength and the ambient galaxy radiation field. We estimate the path length to be $l = R\cos i + H\sin i$, where R is half of the physical galaxy semi-major axis (determined from the angular size and distance scale), and i is the estimated inclination. For galaxies with no detected disk to indicate orientation, we assume $i = 0$.

We find that the calculated L_{dust} does not exceed the observed 24 μm luminosity in the majority (83%) of cases. Of the 15 sources with excess calculated L_{dust} compared to the observed SED, only one is inconsistent with AGN variability observed for a similar sample on year-long timescales (Sarajedini et al. 2006). That source, S160, has an uncharacteristically low 24 μm luminosity compared to the rest of our sample. We conclude that the selected parameters of U and l do not greatly over- or underestimate the reprocessed AGN dust emission of our sample. However, the assumption that reddening of the optical point source is due entirely to dust from an AGN torus means that the calculated L_{dust} should be considered an upper limit.

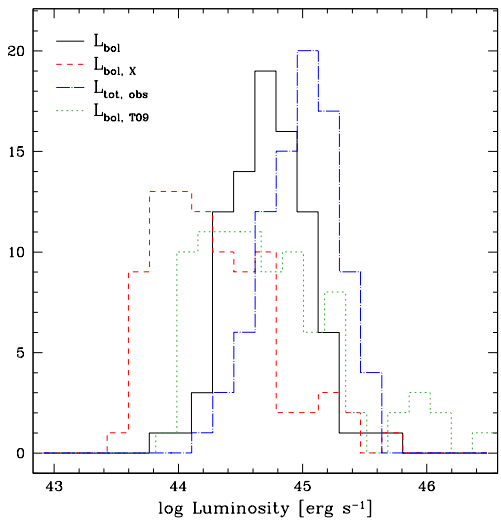

FIG. 6.— Histograms of bolometric luminosities calculated four ways: (1) using our SED-reddening fit method from Section 4.2, L_{bol} (black solid line); (2) using our empirical bolometric correction to the X-ray luminosity, $L_{bol,X}$ (red, dashed line); (3) using a simple sum of all the observed light for each source, $L_{\rm tot,obs}$ (blue, dot-dashed line); and (4) using the model-based, luminosity-dependent correction of Treister et al. (2009), $L_{bol,\rm T09}$ (green, dotted line). The first method has the smallest scatter and agrees well with the successful population synthesis model of Treister et al.; the second method underestimates the luminosity, probably because a significant fraction of the X-rays are absorbed; and the third method overestimates L_{bol} because of a significant contribution from the host galaxy. A Kolmogorov-Smirnov (K-S) test indicates a 6.3% chance that the distributions of L_{bol} and $L_{bol,\rm T09}$ are from the same parent distribution, whereas there is less than a 0.001% chance that the L_{bol} distribution is consistent with either the $L_{bol,X}$ or $L_{\rm tot,obs}$ distributions.

4.3. *Comparison of Bolometric Luminosity Methods*

Figure 6 shows a comparison between the bolometric luminosities calculated four ways: (1) by integrating the complete AGN SED we constructed for each object as described in Section 4.2, L_{bol}; (2) by estimating an X-ray correction using the mean broad-line AGN SEDs calculated in Section 4.1, $L_{bol,X}$; (3) by summing the source luminosity in all observed bands, $L_{\rm tot,obs}$; and (4) by using model-derived, luminosity-dependent bolometric corrections to the X-ray luminosity ($L_{bol,\rm T09}$; Treister et al. 2009).

For the relatively small number of objects (6) in our sample with $L_X > 10^{44}$ erg s^{-1}, using our point-source fitting method to calculate L_{bol} has close to the same result as simply adding up the total luminosity in the source SED. However, the rest of our sources are dominated by the host galaxy in the optical and infrared wavelengths, leading to a significant overestimation of AGN-only luminosity with a simple summation method. For our entire sample, the mean value of $L_{\rm tot,obs}$ is too large by approximately 80% compared to the mean L_{bol} computed using our point-source fitting method.

In contrast, the simple bolometric correction computed in Section 4.1 is too low by 66% on average. This is unsurprising, because our correction is derived from an observed SED that lacks FIR data at longer wavelengths than 24 μm (observed), which can contribute significantly to the observed total luminosity. This is exacerbated when applying a correction to objects like those in our main sample, whose X-ray luminosity has been subject to circumnuclear absorption. Using the Draine (2003) dust models to estimate this FIR component in the broad-line AGN increases the value of the correction from Section 4.1 to a value consistent with Elvis et al. (2002), which increases the corrected luminosities, $L_{bol,X}$, to a mean value more consistent with the mean L_{bol}, but with a larger scatter (σ for $\log L_{bol,X} = 0.46$ compared to 0.33 for $\log L_{bol}$).

Both $L_{bol,X}$ and $L_{\rm tot,obs}$ are calculated using observed properties. We assess the accuracy of our L_{bol} calculation, which combines observations with model-dependent parameters, by comparing to an independent theoretical model. Specifically, we use the luminosity-dependent bolometric corrections calculated in Treister et al. (2009) for model AGN SEDs with a range of X-ray luminosities, column densities, and orientations (Treister et al. 2006). Using the absorption-corrected X-ray luminosity of each object in our main sample to predict a bolometric correction yields a bolometric luminosity for each object, $L_{bol,\rm T09}$.

Encouragingly, the mean values of $L_{bol,\rm T09}$ and L_{bol} are in good agreement ($\log\langle L_{bol,\rm T09}\rangle = 44.75 \pm 0.55$ and $\log\langle L_{bol}\rangle = 44.74 \pm 0.33$), with the distribution of $L_{bol,\rm T09}/L_{bol}$ having a peak and width (σ) of 1.0 ± 0.8. This indicates that the prediction of the Treister et al. (2009) model generally agrees well with calculations of L_{bol} for individual objects. Such strong agreement for two completely independent ways of calculating bolometric luminosities implies that the observed reddening of the central point source is dominated by absorption processes occurring within the circumnuclear region.

Individual-source bolometric luminosities for each of the four methods are presented in Table 2. Note that, compared to L_{bol} (method 1), $L_{bol,X}$ (method 2) underestimates the bolometric luminosity and $L_{\rm tot,obs}$ (method 3) overestimates it. Both $L_{bol,X}$ and $L_{bol,\rm T09}$ (method 4) distributions have more scatter, which suggests the point-source fitting method (method 1) may be superior. We use this value, L_{bol}, in the subsequent analysis.

Figure 7 shows the distribution of L_{bol} with redshift, as well as the ratio of L_{bol} to the observed L_X. We detect no trend in L_{bol} with redshift, but the objects with lower L_X appear to have a higher scatter in L_{bol} compared to objects with higher L_X. Interestingly, values of L_{bol} calculated using point-source luminosities in only 1 or 2 optical bands, while individually more uncertain than values calculated with 3 or 4 bands of optical point-source data, are not outliers in the overall distribution of L_{bol}. This suggests that a sample of AGN with L_{bol} calculated as in section 4.2, but with only one optical band used to determine $E(B-V)$, may be reliable as a sample even if the individual values have high uncertainty.

4.4. *Dust-to-Gas Ratios*

Our point-source fitting method produces estimates of $E(B-V)$ from optical point-source dust reddening. We also have gas column density (N_H) measurements from X-ray spectral slope fitting. These two quantities allow for an independent measurement of the intrinsic dust-to-gas ratio in AGN. Figure 8 shows the measures of dust vs. gas in the form of $E(B-V)$ vs. N_H. Binning the data in Figure 8 over four N_H ranges shows no strong trend; however, a Kolmogorov-Smirov (K-S)

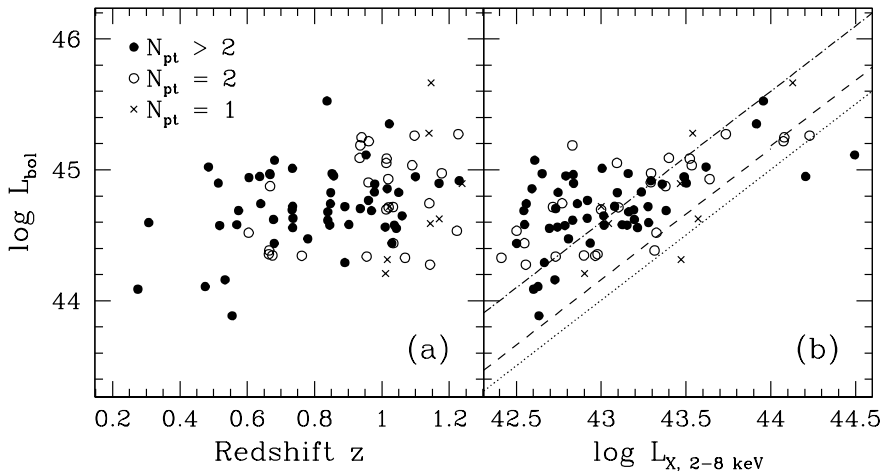

FIG. 7.— Calculated bolometric luminosities and comparison of methods. Panels show: (a) Bolometric luminosity (L_{bol}), as described in Section 4.2 (method 1 in Figure 6), versus redshift. Solid points indicate objects with nuclear point source detections in at least 3 optical bands ($N_{pt} > 2$); open circles show sources with $N_{pt} = 2$; crosses show sources with $N_{pt} = 1$, which have highly uncertain values of $E(B-V)$ and thus L_{bol}. We detect no trend in L_{bol} with redshift. (b) Bolometric luminosity versus absorption-corrected hard X-ray luminosity. Fixed bolometric corrections of $L_{bol} = 10 \times L_X$ (dotted line; Elvis et al. 1994) or $L_{bol} \approx 15 \times L_X$ (dashed line; Section 4.1) underestimate L_{bol}. The peak of the L_{bol}/L_X distribution ($(L_{bol}/L_X)_{\rm peak} = 39.5$) is shown as a dot-dashed line and is likely higher than corrections based on unobscured AGN because of significant X-ray absorption in this sample.

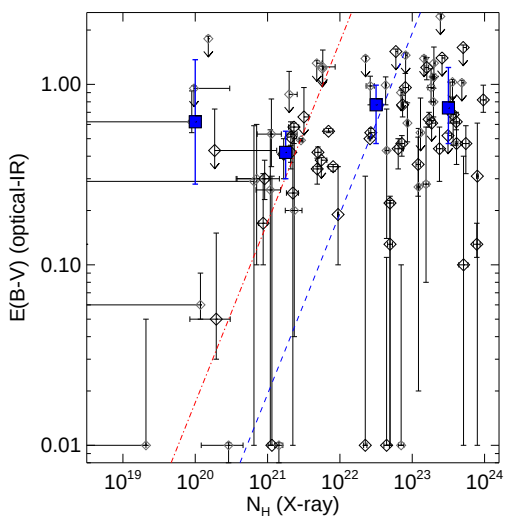

FIG. 8.— $E(B-V)$ derived from dust reddened model SED fits vs. X-ray-determined gas column density. Larger diamonds indicate $E(B-V)$ calculated using at least 3 ACS filters; smaller points indicate that the $E(B-V)$ calculation used only one or 2 filters. Average values for four N_H bins (*blue squares*) show no strong trend: intrinsically obscured AGN ($N_H > 10^{22}$ cm^{-2}) tend towards larger reddening coefficients, but not universally. The ratios span a wide range, from approximately that of the SMC (*red dot-dash*, $E(B-V)/N_H = 2.2 \times 10^{-23}$ cm^2/H) to ratios in excess of Galactic (*blue dashed*, $E(B-V)/N_H = 1.7 \times 10^{-22}$ cm^2/H).

test indicates only a 0.4% chance that the subsample of $E(B-V)$ values for objects with $N_H < 10^{22}$ cm^{-2} is drawn from the same parent sample as the subsample of $E(B-V)$ values for objects with $N_H > 10^{22}$ cm^{-2}. This indicates that dust and gas obscuration may be weakly correlated, so that sources with higher N_H tend toward higher $E(B-V)$ values, but with large scatter. The dust-to-gas ratios span a relatively wide range, including dust-to-gas ratios similar to the Galactic value, $E(B-V)/N_H = 1.7 \times 10^{-22}$ cm^2/H (see Draine 2003; Shull & van Steenberg 1985), and those closer to that in the SMC, $E(B-V)/N_H = 2.2 \times 10^{-23}$ cm^2/H (Martin et al. 1989).

The SMC-like dust ratios are consistent with observations of local Seyferts, based on their star formation histories and intrinsic metallicities (Maiolino et al. 2001; Willott et al. 2004; Hopkins et al. 2004). However, as discussed in Willott et al. (2004), the similarity of these dust-to-gas ratios is likely a coincidence, due to the drastically different physical conditions between AGN and the SMC. Maiolino et al. (2001, 1997) discuss at least three causes for the much higher gas-to-dust ratio relative to the Milky Way: (1) a difference in dust grain composition and size such that UV absorption is less effective; (2) the ratio of dust to gas is simply lower than in our galaxy; and (3) an effect of the majority of X-ray absorption occurring very close to the ionizing radiation and within the dust sublimation radius (defined at roughly 1500 K, and on the order of $R_{sub} = 0.1 - 1$ pc). The work of Elitzur & Shlosman (2006) supports this last explanation.

The majority (90%) of our sample lack detected broad emission lines, which within the AGN unification paradigm is commonly interpreted as the result of an optically thick line-of-sight to the broad-line region (also within the dust sublimation radius; Hönig et al. 2006). This, combined with the high obscuration for much of our sample, suggests most of the gas and dust along the line of sight lies within the X-ray dissociation region.

5. EDDINGTON RATIOS

The use of hard X-ray luminosity to select a complete sample of AGN is vital to studies of AGN accretion properties. Approximately 90% of our sources would fail to be included in samples selected by optical spectroscopy. Additionally, the use of *HST* data allows for black hole mass estimates that are independent of AGN proper-

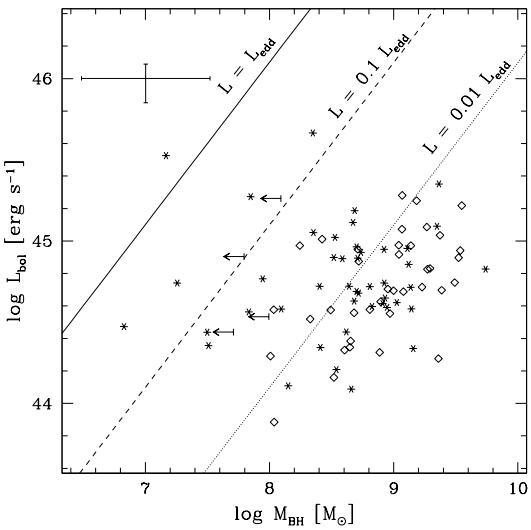

FIG. 9.— Bolometric AGN luminosity vs. black hole mass. Bulge-dominated (*diamonds*) and disk-dominated systems (*stars*) have overlapping distributions, although most of the lowest-mass black holes are in disk-dominated systems. Typical errors are indicated at the upper left. Lines show 100%, 10%, and 1% of the Eddington ratio; the mean and median Eddington ratios for our sample are $L = 0.009 \times L_{Edd}$ and $L = 0.006 \times L_{Edd}$, respectively.

ties. Most AGN host galaxies are unresolved in black hole surveys selected by broad $H\beta$ (Kollmeier et al. 2006; Vestergaard & Peterson 2006; Bentz et al. 2006), [O III] (Netzer et al. 2007a) or CIV emission lines (Vestergaard 2002; Kaspi et al. 2005). Conversely, most of the optical spectra in narrow-line AGN (Barger et al. 2003; Cowie et al. 2003; Szokoly et al. 2004) are good enough for redshifts, but lack the signal-to-noise for a measurement of $M_\bullet$ (*e.g.*, Heckman et al. 2004). Our X-ray selection criteria, combined with not being dependent on line widths for $M_\bullet$ estimates, allows us to examine AGN that are not individually contributing strongly to the accretion history of AGN, but that are a significant fraction of the X-ray luminosity function (and hence total black hole accretion) at intermediate redshifts.

Figure 9 shows the comparison between the black hole mass (Section 3) and bolometric luminosity (Section 4.2). The mean and median Eddington ratios for our sample are $\langle L_{bol}/L_{Edd}\rangle = 0.009$ and 0.006, respectively (where $L_{Edd} \equiv 1.3 \times 10^{38}(M_\bullet/M_\odot)$ erg s^{-1}), meaning the majority of the sample consists of AGN with highly sub-Eddington accretion rates. Only one-third of the sample has $L_{bol}/L_{Edd} > 0.01$. This result – a typically low Eddington ratio within a sample that spans a wide range of values – is similar to results for local Seyfert galaxies (*e.g.*, Cardamone et al. 2007; Mushotzky et al. 2008).

The scarcity of AGN with high accretion rates is at least partly to be expected from our selection criteria. By excluding AGN with low host-to-point source luminosity ratios, we preferentially exclude high-Eddington-ratio black holes for all but the smallest SMBH. Our selection process (§2.1) rejects 34 AGN+hosts in total, of which 16 are too faint to accurately recover bulge luminosities. Given their low fluxes, those 16 objects are unlikely to be bright, near-Eddington accreting AGN. The other 18 rejected objects are point-like in the optical images, which could possibly be due to bright (near-Eddington-accreting) nuclei. However, even if those objects were included, they would constitute a minority of the total sample, indicating that our sample of sub-Eddington AGN represents the dominant AGN population within the GOODS fields at $z < 1.25$.

The result that more than 90% of our sample is accreting at less than 10% of the Eddington limit is robust to possible sources of error in our analysis. If we were to assume that our sources are accreting at the Eddington limit and use that assumption to calculate SMBH masses, our masses would decrease by more than two orders of magnitude, on average. Such a large deviation is inconsistent both with independent observations of black hole masses and bulges from $0 \lesssim z \lesssim 3$ (*e.g.*, Woo et al. 2008; Jahnke et al. 2009; Merloni et al. 2010) and with constraints on the maximum evolution of the black hole-bulge relation from studies that *do* assume Eddington-limited accretion (Borys et al. 2005; Bluck et al. 2011). Our results are also inconsistent with scenarios in which most SMBHs cycle between a fully quiescent state and a near-Eddington accretion state (*e.g.*, King 2010). Even assuming the largest possible deviation in black hole masses based on the maximum evolution of the bulge-black hole relation, our AGN are still in a phase of very slow growth.

The Eddington ratios are presented in Figure 10 in relation to $M_\bullet$ and redshift. To determine whether we see any significant evolution of Eddington ratios (as others have; *e.g.,* Netzer & Trakhtenbrot 2007; Greene & Ho 2007), we consider the relevant selection biases. In Figure 10, we plot the hard X-ray luminosity limit ($L_X > 3 \times 10^{42}$ erg s^{-1}, dashed line) of our sample, which excludes low Eddington ratio, low mass AGN. At the same time, high-luminosity AGN are sufficiently rare that they do not appear in pencil-beam surveys such as GOODS; we show this by plotting in Figure 10 the luminosity at which we expect to detect only 1 AGN within the GOODS volume (which is a function of redshift) from the quasar luminosity function (Croom et al. 2004). After accounting for these selection effects, we detect no correlation between Eddington ratio and either black hole mass or redshift. This lack of real trend is consistent with Woo & Urry (2002), who found that selection effects can create the appearance of correlations where none intrinsically exist.

Our values of L_{bol}/L_{Edd} are somewhat lower than those reported by others (Kollmeier et al. 2006; Greene & Ho 2007; Netzer et al. 2007b). Direct comparison between different studies is complicated, however, due to the varying selection criteria, redshifts and flux limits of each study. For example, restricting a comparison to the objects in their paper with redshifts similar to ours, Kollmeier et al. (2006) find that the broad-line AGN from the AGES survey (Kochanek et al. 2004) radiate at near-Eddington rates, $0.1 < \lambda < 1.0$. But their study has considerably brighter flux limits than our own, with AGES being 50% complete at $R = 21.5$, whereas our sample is nearly complete down to $z_{850} = 24.0$ under the constraints outlined in Sections 2.1 and 2.2. Direct comparison to the large, optically-selected SDSS quasar sample (Schneider et al. 2007) is also difficult owing to that sample being highly incomplete at low Eddington ratios (Kelly et al. 2010). Samples with similar selection crite-

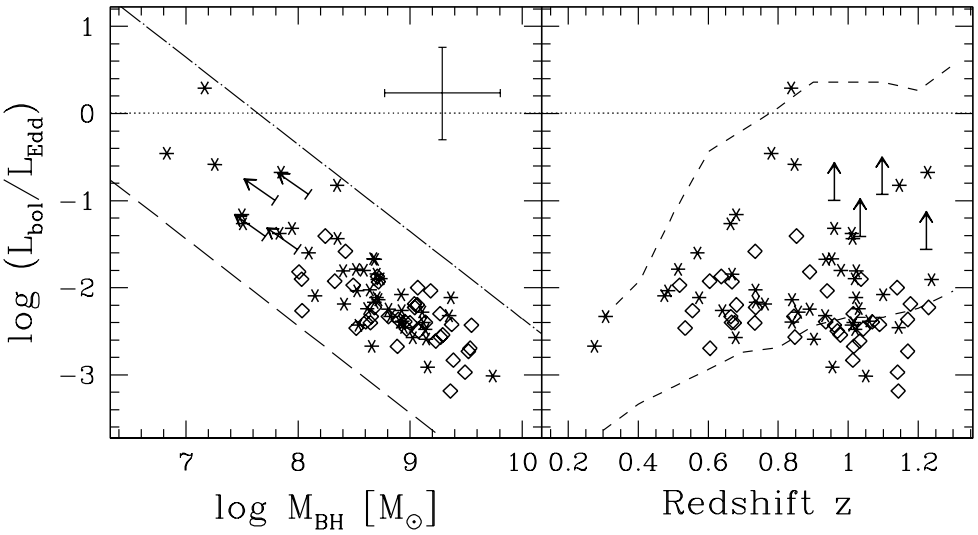

FIG. 10.— Eddington ratio vs. black hole mass (*left*) and redshift (*right*). Symbols indicate bulge-like (*diamonds*) and disk-like (*stars*) host galaxy morphologies. The dashed line in the left panel indicates the lower L_X selection criteria of 3×10^{42} erg s^{-1}, and the dot-dashed line indicates the upper luminosity limit for a single-source detection based on the Croom et al. (2004) quasar luminosity function calculated for the GOODS area. The dashed lines on the right indicate the maximum and minimum luminosities of X-ray sources detected in the GOODS parent sample at each redshift, assuming $\log M_\bullet = 7.0 M_\odot$. In both panels, the observations more or less fill the allowed area.

ria and flux limits (Bundy et al. 2008), and those with overlapping samples from the same survey (Ballo et al. 2007), report Eddington ratios more similar to ours.

Interestingly, many of the aforementioned black hole samples at different redshifts and with different selection criteria do not appear to have radically different accretion rates. Greene & Ho (2007) show that a sample of broad-line AGN selected from the SDSS have a peak black hole mass of $10^7 M_\odot$ at $z < 0.3$, with a typical Eddington rate of 10%, or a typical accretion rate of $2\times10^{-3}/\epsilon\ M_\odot$ yr^{-1}, where ϵ is the efficiency of converting mass to light. Most AGN in our sample have similar accretion rates (to within 40%), despite having higher masses and lower Eddington rates. Our accretion rates are consistent with those of Ballo et al. (2007) sample, which overlaps ours somewhat, even though they calculate $M_\bullet$ and L_{bol} differently. Type 1 AGN from the zCOSMOS sample (Merloni et al. 2010), which probes higher redshifts and luminosities than our GOODS sample, are accreting at rate higher than ours by only a factor of ~ 4. And Hickox et al. (2009), who probe a slightly lower-mass part of the black-hole mass function at similar redshifts, find that black holes in AGN are accreting at a rate within a factor of 2 of ours. These different samples of AGN span a wide range of redshifts, luminosities, and black hole masses, yet they have similar estimates of accretion rates in $M_\odot$ yr^{-1}, assuming the same radiative efficiency. This suggests that the accretion rates of AGN may be more directly related to the supply of material from the circumnuclear region than the properties of the central black hole.

If we follow Elvis et al. (2002) and assume a minimum radiative efficiency of $\epsilon = 0.15$, our median black hole with an Eddington ratio of 0.006 and mass of $5.1\times10^8 M_\odot$ is accreting at $\dot{M} \sim 0.05\ M_\odot$ yr^{-1}. This accretion rate is too low to have been the typical rate for the duration of the AGN activity cycle: given our median redshift, it would take a seed black hole a minimum of $\sim 150\%$ of the age of the universe to that point to have grown to its present size, assuming growth from the largest initial mass of direct-collapse black holes (Volonteri et al. 2008), $\sim 10^6\ M_\odot$. Given that the seed mass is likely to have been lower, and that this accretion rate is super-Eddington for $M_\bullet \lesssim 3\times10^6\ M_\odot$, the actual time would likely be far higher. For any reasonable assumptions, therefore, the accretion rate of a typical black hole in our sample must have been significantly higher at some point in the past in order for it to grow to its present size within a Hubble time. Assuming a larger radiative efficiency, which Elvis et al. suggest is possible, only strengthens this conclusion.

This is unsurprising given that black hole growth scenarios involving a period of rapid (Eddington-limited) growth followed by a power-law-decay growth rate (*e.g.*, Hopkins et al. 2006; Yu & Lu 2008) are more consistent with observations of Eddington ratio distributions in a complete sample than constant-growth or "light bulb" scenarios (Hopkins & Hernquist 2009). Under the specific timescales for a self-regulating feedback model described in Hopkins & Hernquist (2009), we calculate that a black hole with our median observed redshift ($z = 0.94$) and Eddington ratio has an accretion rate that peaks at $z \approx 1.1$, assuming a single episode of growth. Such an object would easily be detected above our flux limits. The progenitor to our median AGN should therefore be detected within our sample at its peak growth stage (*i.e.*, accreting at a high Eddington ratio). Extending these calculations to each individual object in our sample, we should detect ≈ 60 progenitor AGN accreting at the Eddington limit (within our limiting redshift, $z < 1.25$).

In fact, we detect only 7 possible candidates: 3 sources consistent with $L_{bol}/L_{Edd} = 1$ within our 1σ uncertainties and 4 sources for which the detected L_{bol}/L_{Edd}

is a lower limit. The number of Eddington-limited AGN in our sample is too low by at least an order of magnitude to be consistent with the predictions of the Hopkins & Hernquist model. We also considered the possibility that the progenitors of the slow-growing AGN within our limiting redshift ($z < 1.25$) were removed from our sample due to their bright nuclei rendering them point-like in the optical images (§2.1). However, not only are there not enough of those objects (18) to account for the predictions of the model, but the redshift distribution of the excluded point-like AGN is actually *lower* than that of the objects within our sample (median $z = 0.84$ vs. 0.94 in the included sample). If these objects were progenitors to our slow-growing AGN, their redshifts would necessarily be higher. Comparing the redshift distribution of expected progenitors from our Monte Carlo simulations to the sample of excluded AGN, we find the same result. We therefore argue that the timescales of the single-episode model in Hopkins & Hernquist (2009) do not describe the accretion history of our AGN. A significant fraction of our observed slow-growing black holes must have had a peak growth epoch beyond our maximum redshift.

Overall, most of the X-ray selected AGN constituting our sample are best described as being AGN with high black hole masses and with low accretion rates, in a slow-growth phase. In order to grow to the sizes we observe, the typical source in our sample must have had a significantly higher accretion rate at some point well before $z \sim 1$. Although a preponderance of slowly growing AGN is qualitatively consistent with self-regulating feedback models in which AGN spend most of their time at low accretion rates, our result is inconsistent with quantitative timescales predicted by common parameterizations of this model. The growth history of black holes is clearly more complex than that described by a single simple model, a conclusion echoed by other studies examining AGN at a variety of different redshifts and luminosities (Kauffmann & Heckman 2009; Merloni et al. 2010; Cardamone et al. 2010; Steinhardt & Elvis 2011).

6. CONCLUSIONS

We studied 87 AGN with $z < 1.25$ from the GOODS survey to understand the fundamental properties of moderate-luminosity obscured AGN that make up most of the X-ray background and thus a large fraction of black hole growth. Most of these AGN would not be selected via broad emission line surveys or blue color excesses, *i.e.*, the highest-L and L/L_{edd} objects are excluded. However, this sample represents the bulk of AGN emission at $z \lesssim 1.25$.

After morphological fits to separate AGN/host galaxy light and determine bulge-to-total ratios, we estimated black hole masses for each AGN using the $M_\bullet - L_B$ relation of Marconi & Hunt (2003) as reformulated by Ferrarese & Ford (2005). We do not assume this relation evolves with redshift, but use a Monte Carlo error analysis to account for uncertainty in the time evolution of Equation 1 as well as other parameter uncertainties. The resulting uncertainties in our black hole masses are typically on the order of 0.5 dex.

Using an unobscured AGN template calculated from broad-line AGN in the GOODS fields, we calculated bolometric luminosities individually for each object by reddening the normalized template SED to match nuclear point-source colors and using the fitted $E(B-V)$ to calculate the energy re-radiated in the far-infrared by dust surrounding the AGN. This method is consistent with single-prescription empirical bolometric correction methods and with independent theoretical models, but has less scatter.

The SED fitting of the nuclear point sources gives the added benefit of an estimate of dust absorption upon the AGN template. Assuming a standard Galactic reddening curve, we find that 70% of the AGN have dust-to-gas ratios similar to local Seyferts (Maiolino et al. 2001). The host galaxy contribution to the nuclear line-of-sight obscuration in the GOODS AGN is minimal for most of our sources.

Our survey reveals a considerable fraction of low-Eddington-accreting, high-black-hole-mass AGN in normal host galaxies. The mean Eddington ratio for our sample is $L/L_{Edd} \sim 0.009^{+0.046}_{-0.005}$, considerably lower than in broad-line AGN surveys such as SDSS (Netzer et al. 2007a; Greene & Ho 2007). Many of these AGN have properties consistent with local Seyfert AGN (Mushotzky et al. 2008). Even considering the small uncertainties in the Eddington ratio, which reflect the current uncertainty in the time evolution of the bulge-black hole mass relation, our typical source is still accreting at well below the Eddington limit.

The observed Eddington ratios of our sources are low, but their black hole masses are high, meaning they must have been accreting at significantly higher rates at some point during their growth history in order for them to have reached their observed masses within a Hubble time. According to self-regulating feedback accretion models for black hole growth, our black holes could be the slow-growth phase of their AGN lifetimes; comparison with accretion timescales from simple models of self-regulated feedback indicate that our AGN sample may have a complex accretion history. A significant fraction of our sample must have been accreting at near-Eddington rates before $z \sim 1$. Such a complex growth history is consistent with the downsizing scenario (Barger et al. 2005; Hasinger et al. 2005).

The use of the point-source luminosity as leverage to extract the multi-wavelength AGN SED from a combined AGN plus host galaxy source is a promising technique. In particular, the high-resolution infrared data promised by *JWST* could be used to significantly increase the accuracy of the central reddening determination, which would decrease uncertainty about the re-radiated dust luminosity in the FIR range. This technique may also benefit from the separation of AGN and host galaxies at IR wavelengths using WFC3 (Schawinski et al. 2011). Although the efficacy of host-point-source separation has not yet been studied in as much depth using WFC3 data as it has for ACS, the addition of several data points to the low-resolution point-source SED would be very valuable.

The authors wish to thank to C. Peng for making `GALFIT` publicly available, and for many enlightening discussions. Thanks also to C. Cardamone and E. Bonning for helpful comments on this manuscript. We appreciate helpful comments from the anonymous referee. The JavaScript Cosmology Calculator was used while prepar-

ing this paper (Wright 2006). The authors acknowledge support from NASA through grants HST-AR-10689.01-A, HST-GO-09425.13-A and HST-GO-09822.09-A from the Space Telescope Science Institute, which is operated by the Association of Universities for Research in Astronomy under NASA contract NAS 5-26555. The authors also acknowledge support from the *XMM-Newton* Grant NNG06GD72G. *XMM-Newton* is an ESA science mission with instruments and contributions directly funded by ESA Member States and the USA (NASA). Support for the work of E.T. was provided by NASA through Chandra Postdoctoral Fellowship grant number PF8-90055, issued by the Chandra X-ray Observatory Center, which is operated by the Smithsonian Astrophysical Observatory for and on behalf of NASA under contract NAS8-03060.

REFERENCES

Alexander, D. M., Bauer, F. E., Brandt, W. N., Schneider, D. P., Hornschemeier, A. E., Vignali, C., Barger, A. J., Broos, P. S., Cowie, L. L., Garmire, G. P., Townsley, L. K., Bautz, M. W., Chartas, G., & Sargent, W. L. W. 2003, AJ, 126, 539
Alexander, D. M., Brandt, W. N., Smail, I., Swinbank, A. M., Bauer, F. E., Blain, A. W., Chapman, S. C., Coppin, K. E. K., Ivison, R. J., & Menéndez-Delmestre, K. 2008, AJ, 135, 1968
Alonso-Herrero, A., Pérez-González, P. G., Rieke, G. H., Alexander, D. M., Rigby, J. R., Papovich, C., Donley, J. L., & Rigopoulou, D. 2008, ApJ, 677, 127
Ballo, L., Cristiani, S., Fasano, G., Fontanot, F., Monaco, P., Nonino, M., Pignatelli, E., Tozzi, P., Vanzella, E., Fontana, A., Giallongo, E., Grazian, A., & Danese, L. 2007, ApJ, 667, 97
Barger, A. J., Cowie, L. L., Capak, P., Alexander, D. M., Bauer, F. E., Fernandez, E., Brandt, W. N., Garmire, G. P., & Hornschemeier, A. E. 2003, AJ, 126, 632
Barger, A. J., Cowie, L. L., Mushotzky, R. F., Yang, Y., Wang, W., Steffen, A. T., & Capak, P. 2005, AJ, 129, 578
Bauer, F. E., Alexander, D. M., Brandt, W. N., Schneider, D. P., Treister, E., Hornschemeier, A. E., & Garmire, G. P. 2004, AJ, 128, 2048
Bentz, M. C., Peterson, B. M., Pogge, R. W., Vestergaard, M., & Onken, C. A. 2006, ApJ, 644, 133
Bertin, E., & Arnouts, S. 1996, A&AS, 117, 393
Bluck, A. F. L., Conselice, C. J., Almaini, O., Laird, E. S., Nandra, K., & Grützbauch, R. 2011, MNRAS, 410, 1174
Borys, C., Smail, I., Chapman, S. C., Blain, A. W., Alexander, D. M., & Ivison, R. J. 2005, ApJ, 635, 853
Bundy, K., Georgakakis, A., Nandra, K., Ellis, R. S., Conselice, C. J., Laird, E., Coil, A., Cooper, M. C., Faber, S. M., Newman, J. A., Pierce, C. M., Primack, J. R., & Yan, R. 2008, ApJ, 681, 931
Cardamone, C. N., Moran, E. C., & Kay, L. E. 2007, AJ, 134, 1263
Cardamone, C. N., Urry, C. M., Schawinski, K., Treister, E., Brammer, G., & Gawiser, E. 2010, ApJ, 721, L38
Cardelli, J. A., Clayton, G. C., & Mathis, J. S. 1989, ApJ, 345, 245
Cowie, L. L., Barger, A. J., Bautz, M. W., Brandt, W. N., & Garmire, G. P. 2003, ApJ, 584, L57
Cowie, L. L., Barger, A. J., Hu, E. M., Capak, P., & Songaila, A. 2004, AJ, 127, 3137
Croom, S. M., Smith, R. J., Boyle, B. J., Shanks, T., Miller, L., Outram, P. J., & Loaring, N. S. 2004, MNRAS, 349, 1397
Decarli, R., Falomo, R., Treves, A., Labita, M., Kotilainen, J. K., & Scarpa, R. 2010, MNRAS, 402, 2453
Draine, B. T. 2003, ApJ, 598, 1017
Draine, B. T., & Li, A. 2007, ApJ, 657, 810
Elitzur, M., & Shlosman, I. 2006, ApJ, 648, L101
Elvis, M., Risaliti, G., & Zamorani, G. 2002, ApJ, 565, L75
Elvis, M., Wilkes, B. J., McDowell, J. C., Green, R. F., Bechtold, J., Willner, S. P., Oey, M. S., Polomski, E., & Cutri, R. 1994, ApJS, 95, 1
Fabian, A. C., & Iwasawa, K. 1999, MNRAS, 303, L34
Ferrarese, L., & Ford, H. 2005, Space Science Reviews, 116, 523
Ferrarese, L., & Ford, H. C. 1999, ApJ, 515, 583
Ford, H. C., Harms, R. J., Tsvetanov, Z. I., Hartig, G. F., Dressel, L. L., Kriss, G. A., Bohlin, R. C., Davidsen, A. F., Margon, B., & Kochhar, A. K. 1994, ApJ, 435, L27
Gabor, J. M., Impey, C. D., Jahnke, K., Simmons, B. D., Trump, J. R., Koekemoer, A. M., Brusa, M., Cappelluti, N., Schinnerer, E., Smolčić, V., Salvato, M., Rhodes, J. D., Mobasher, B., Capak, P., Massey, R., Leauthaud, A., & Scoville, N. 2009, ApJ, 691, 705
Genzel, R., Eckart, A., Ott, T., & Eisenhauer, F. 1997, MNRAS, 291, 219
Ghez, A. M., Salim, S., Hornstein, S. D., Tanner, A., Lu, J. R., Morris, M., Becklin, E. E., & Duchêne, G. 2005, ApJ, 620, 744
Giacconi, R., Zirm, A., Wang, J., Rosati, P., Nonino, M., Tozzi, P., Gilli, R., Mainieri, V., Hasinger, G., Kewley, L., Bergeron, J., Borgani, S., Gilmozzi, R., Grogin, N., Koekemoer, A., Schreier, E., Zheng, W., & Norman, C. 2002, ApJS, 139, 369
Giavalisco, M., et al. 2004, ApJ, 600, L93
Greene, J. E., & Ho, L. C. 2007, ApJ, 667, 131
Greenhill, L. J., Kondratko, P. T., Lovell, J. E. J., Kuiper, T. B. H., Moran, J. M., Jauncey, D. L., & Baines, G. P. 2003, ApJ, 582, L11
Grogin, N. A., Koekemoer, A. M., Schreier, E. J., Bergeron, J., Giacconi, R., Hasinger, G., Kewley, L., Norman, C., Rosati, P., Tozzi, P., & Zirm, A. 2003, ApJ, 595, 685
Hasinger, G., Miyaji, T., & Schmidt, M. 2005, A&A, 441, 417
Heckman, T. M., Kauffmann, G., Brinchmann, J., Charlot, S., Tremonti, C., & White, S. D. M. 2004, ApJ, 613, 109
Herrnstein, J. R., Moran, J. M., Greenhill, L. J., Diamond, P. J., Inoue, M., Nakai, N., Miyoshi, M., Henkel, C., & Riess, A. 1999, Nature, 400, 539
Hickox, R. C., Jones, C., Forman, W. R., Murray, S. S., Kochanek, C. S., Eisenstein, D., Jannuzi, B. T., Dey, A., Brown, M. J. I., Stern, D., Eisenhardt, P. R., Gorjian, V., Brodwin, M., Narayan, R., Cool, R. J., Kenter, A., Caldwell, N., & Anderson, M. E. 2009, ApJ, 696, 891
Hönig, S. F., Beckert, T., Ohnaka, K., & Weigelt, G. 2006, A&A, 452, 459
Hopkins, P. F., & Hernquist, L. 2009, ApJ, 698, 1550
Hopkins, P. F., Hernquist, L., Cox, T. J., Robertson, B., Di Matteo, T., & Springel, V. 2006, ApJ, 639, 700
Hopkins, P. F., Richards, G. T., & Hernquist, L. 2007, ApJ, 654, 731
Hopkins, P. F., Strauss, M. A., Hall, P. B., Richards, G. T., Cooper, A. S., Schneider, D. P., Vanden Berk, D. E., Jester, S., Brinkmann, J., & Szokoly, G. P. 2004, AJ, 128, 1112
Jahnke, K., Bongiorno, A., Brusa, M., Capak, P., Cappelluti, N., Cisternas, M., Civano, F., Colbert, J., Comastri, A., Elvis, M., Hasinger, G., Ilbert, O., Impey, C., Inskip, K., Koekemoer, A. M., Lilly, S., Maier, C., Merloni, A., Riechers, D., Salvato, M., Schinnerer, E., Scoville, N. Z., Silverman, J., Taniguchi, Y., Trump, J. R., & Yan, L. 2009, ApJ, 706, L215
Kaspi, S., Maoz, D., Netzer, H., Peterson, B. M., Vestergaard, M., & Jannuzi, B. T. 2005, ApJ, 629, 61
Kauffmann, G., & Heckman, T. M. 2009, MNRAS, 397, 135
Kelly, B. C., Vestergaard, M., Fan, X., Hopkins, P., Hernquist, L., & Siemiginowska, A. 2010, ApJ, 719, 1315
King, A. R. 2010, MNRAS, 408, L95
Kochanek, C. S., Eisenstein, D., Caldwell, N., Cool, R., Green, P., & AGES. 2004, in Bulletin of the American Astronomical Society, Vol. 36, Bulletin of the American Astronomical Society, 1495–+
Koekemoer, A. M., Fruchter, A. S., Hook, R. N., & Hack, W. 2002, in The 2002 HST Calibration Workshop : Hubble after the Installation of the ACS and the NICMOS Cooling System, Proceedings of a Workshop held at the Space Telescope Science Institute, Baltimore, Maryland, October 17 and 18, 2002. Edited by Santiago Arribas, Anton Koekemoer, and Brad Whitmore. Baltimore, MD: Space Telescope Science Institute, 2002., p.337, ed. S. Arribas, A. Koekemoer, & B. Whitmore, 337–+

Kollmeier, J. A., Onken, C. A., Kochanek, C. S., Gould, A., Weinberg, D. H., Dietrich, M., Cool, R., Dey, A., Eisenstein, D. J., Jannuzi, B. T., Le Floc'h, E., & Stern, D. 2006, ApJ, 648, 128
Krist, J. 1993, in Astronomical Society of the Pacific Conference Series, Vol. 52, Astronomical Data Analysis Software and Systems II, ed. R. J. Hanisch, R. J. V. Brissenden, & J. Barnes, 536–+
La Franca, F., Fiore, F., Comastri, A., Perola, G. C., Sacchi, N., Brusa, M., Cocchia, F., Feruglio, C., Matt, G., Vignali, C., Carangelo, N., Ciliegi, P., Lamastra, A., Maiolino, R., Mignoli, M., Molendi, S., & Puccetti, S. 2005, ApJ, 635, 864
Mainieri, V., Rosati, P., Tozzi, P., Bergeron, J., Gilli, R., Hasinger, G., Nonino, M., Lehmann, I., Alexander, D. M., Idzi, R., Koekemoer, A. M., Norman, C., Szokoly, G., & Zheng, W. 2005, A&A, 437, 805
Maiolino, R., Marconi, A., Salvati, M., Risaliti, G., Severgnini, P., Oliva, E., La Franca, F., & Vanzi, L. 2001, A&A, 365, 28
Maiolino, R., Ruiz, M., Rieke, G. H., & Papadopoulos, P. 1997, ApJ, 485, 552
Marconi, A., & Hunt, L. K. 2003, ApJ, 589, L21
Marconi, A., Risaliti, G., Gilli, R., Hunt, L. K., Maiolino, R., & Salvati, M. 2004, MNRAS, 351, 169
Martin, N., Maurice, E., & Lequeux, J. 1989, A&A, 215, 219
Mathis, J. S., Mezger, P. G., & Panagia, N. 1983, A&A, 128, 212
Merloni, A., Bongiorno, A., Bolzonella, M., Brusa, M., Civano, F., Comastri, A., Elvis, M., Fiore, F., Gilli, R., Hao, H., Jahnke, K., Koekemoer, A. M., Lusso, E., Mainieri, V., Mignoli, M., Miyaji, T., Renzini, A., Salvato, M., Silverman, J., Trump, J., Vignali, C., Zamorani, G., Capak, P., Lilly, S. J., Sanders, D., Taniguchi, Y., Bardelli, S., Carollo, C. M., Caputi, K., Contini, T., Coppa, G., Cucciati, O., de la Torre, S., de Ravel, L., Franzetti, P., Garilli, B., Hasinger, G., Impey, C., Iovino, A., Iwasawa, K., Kampczyk, P., Kneib, J., Knobel, C., Kovač, K., Lamareille, F., Le Borgne, J., Le Brun, V., Le Fèvre, O., Maier, C., Pello, R., Peng, Y., Perez Montero, E., Ricciardelli, E., Scodeggio, M., Tanaka, M., Tasca, L. A. M., Tresse, L., Vergani, D., & Zucca, E. 2010, ApJ, 708, 137
Miyoshi, M., Moran, J., Herrnstein, J., Greenhill, L., Nakai, N., Diamond, P., & Inoue, M. 1995, Nature, 373, 127
Mushotzky, R. F., Winter, L. M., McIntosh, D. H., & Tueller, J. 2008, ApJ, 684, L65
Netzer, H., Lira, P., Trakhtenbrot, B., Shemmer, O., & Cury, I. 2007a, ApJ, 671, 1256
Netzer, H., Lutz, D., Schweitzer, M., Contursi, A., Sturm, E., Tacconi, L. J., Veilleux, S., Kim, D.-C., Rupke, D., Baker, A. J., Dasyra, K., Mazzarella, J., & Lord, S. 2007b, ApJ, 666, 806
Netzer, H., & Trakhtenbrot, B. 2007, ApJ, 654, 754
Peng, C. Y., Ho, L. C., Impey, C. D., & Rix, H.-W. 2002, AJ, 124, 266
Peng, C. Y., Impey, C. D., Ho, L. C., Barton, E. J., & Rix, H.-W. 2006, ApJ, 640, 114
Persic, M., Rephaeli, Y., Braito, V., Cappi, M., Della Ceca, R., Franceschini, A., & Gruber, D. E. 2004, A&A, 419, 849
Peterson, B. M. 1993, PASP, 105, 247
Peterson, B. M., & Wandel, A. 2000, ApJ, 540, L13
Pierce, C. M., Lotz, J. M., Laird, E. S., Lin, L., Nandra, K., Primack, J. R., Faber, S. M., Barmby, P., Park, S. Q., Willner, S. P., Gwyn, S., Koo, D. C., Coil, A. L., Cooper, M. C., Georgakakis, A., Koekemoer, A. M., Noeske, K. G., Weiner, B. J., & Willmer, C. N. A. 2007, ApJ, 660, L19
Pierce, C. M., Lotz, J. M., Primack, J. R., Rosario, D. J. V., Griffith, R. L., Conselice, C. J., Faber, S. M., Koo, D. C., Coil, A. L., Salim, S., Koekemoer, A. M., Laird, E. S., Ivison, R. J., & Yan, R. 2010a, MNRAS, 405, 718
Pierce, C. M., Lotz, J. M., Salim, S., Laird, E. S., Coil, A. L., Bundy, K., Willmer, C. N. A., Rosario, D. J. V., Primack, J. R., & Faber, S. M. 2010b, MNRAS, 408, 139
Richards, G. T., Lacy, M., Storrie-Lombardi, L. J., Hall, P. B., Gallagher, S. C., Hines, D. C., Fan, X., Papovich, C., Vanden Berk, D. E., Trammell, G. B., Schneider, D. P., Vestergaard, M., York, D. G., Jester, S., Anderson, S. F., Budavári, T., & Szalay, A. S. 2006, ApJS, 166, 470
Sánchez, S. F., Jahnke, K., Wisotzki, L., McIntosh, D. H., Bell, E. F., Barden, M., Beckwith, S. V. W., Borch, A., Caldwell, J. A. R., Häussler, B., Jogee, S., Meisenheimer, K., Peng, C. Y., Rix, H.-W., Somerville, R. S., & Wolf, C. 2004, ApJ, 614, 586
Sanders, D. B., Soifer, B. T., Elias, J. H., Madore, B. F., Matthews, K., Neugebauer, G., & Scoville, N. Z. 1988, ApJ, 325, 74
Sarajedini, V. L., Koo, D. C., Phillips, A. C., Kobulnicky, H. A., Gebhardt, K., Willmer, C. N. A., Vogt, N. P., Laird, E., Im, M., Iverson, S., & Mattos, W. 2006, ApJS, 166, 69
Schawinski, K., Treister, E., Urry, C. M., Cardamone, C. N., Simmons, B., & Yi, S. K. 2011, ApJ, 727, L31+
Schneider, D. P., Hall, P. B., Richards, G. T., Strauss, M. A., Vanden Berk, D. E., Anderson, S. F., Brandt, W. N., Fan, X., Jester, S., Gray, J., Gunn, J. E., SubbaRao, M. U., Thakar, A. R., Stoughton, C., Szalay, A. S., Yanny, B., York, D. G., Bahcall, N. A., Barentine, J., Blanton, M. R., Brewington, H., Brinkmann, J., Brunner, R. J., Castander, F. J., Csabai, I., Frieman, J. A., Fukugita, M., Harvanek, M., Hogg, D. W., Ivezić, Ž., Kent, S. M., Kleinman, S. J., Knapp, G. R., Kron, R. G., Krzesiński, J., Long, D. C., Lupton, R. H., Nitta, A., Pier, J. R., Saxe, D. H., Shen, Y., Snedden, S. A., Weinberg, D. H., & Wu, J. 2007, AJ, 134, 102
Shull, J. M., & van Steenberg, M. E. 1985, ApJ, 294, 599
Simmons, B. D., & Urry, C. M. 2008, ApJ, 683, 644
Spergel, D. N., Verde, L., Peiris, H. V., Komatsu, E., Nolta, M. R., Bennett, C. L., Halpern, M., Hinshaw, G., Jarosik, N., Kogut, A., Limon, M., Meyer, S. S., Page, L., Tucker, G. S., Weiland, J. L., Wollack, E., & Wright, E. L. 2003, ApJS, 148, 175
Steinhardt, C. L., & Elvis, M. 2011, MNRAS, 410, 201
Szokoly, G. P., et al. 2004, ApJS, 155, 271
Taylor, E. N., Franx, M., van Dokkum, P. G., Quadri, R. F., Gawiser, E., Bell, E. F., Barrientos, L., Blanc, G. A., Castander, F. J., Damen, M., Gonzalez-Perez, V., Hall, P. B., Herrera, D., Hildebrandt, H., Kriek, M., Labbé, I., Lira, P., Maza, J., Rudnick, G., Treister, E., Urry, C., Willis, J. P., & Wuyts, S. 2009, ArXiv e-prints
Treister, E., Krolik, J. H., & Dullemond, C. 2008, ApJ, 679, 140
Treister, E., & Urry, C. M. 2005, ApJ, 630, 115
—. 2006, ApJ, 652, L79
Treister, E., Urry, C. M., Van Duyne, J., Dickinson, M., Chary, R.-R., Alexander, D. M., Bauer, F., Natarajan, P., Lira, P., & Grogin, N. A. 2006, ApJ, 640, 603
Treister, E., Urry, C. M., & Virani, S. 2009, ApJ, 696, 110
Treister, E., et al. 2004, ApJ, 616, 123
Treu, T., Malkan, M. A., & Blandford, R. D. 2004, ApJ, 615, L97
Ueda, Y., Akiyama, M., Ohta, K., & Miyaji, T. 2003, ApJ, 598, 886
Vestergaard, M. 2002, ApJ, 571, 733
Vestergaard, M., & Peterson, B. M. 2006, ApJ, 641, 689
Volonteri, M., Lodato, G., & Natarajan, P. 2008, MNRAS, 383, 1079
Willott, C. J., Simpson, C., Almaini, O., Johnson, O., Lawrence, A., Dunlop, J. S., Roche, N. D., Mann, R. G., Manners, J. C., González-Solares, E., Pérez-Fournon, I., Ivison, R. J., Serjeant, S., Oliver, S. J., McMahon, R. G., & Rowan-Robinson, M. 2004, ApJ, 610, 140
Wirth, G. D., Willmer, C. N. A., Amico, P., Chaffee, F. H., Goodrich, R. W., Kwok, S., Lyke, J. E., Mader, J. A., Tran, H. D., Barger, A. J., Cowie, L. L., Capak, P., Coil, A. L., Cooper, M. C., Conrad, A., Davis, M., Faber, S. M., Hu, E. M., Koo, D. C., Le Mignant, D., Newman, J. A., & Songaila, A. 2004, AJ, 127, 3121
Woo, J., Treu, T., Malkan, M. A., & Blandford, R. D. 2008, ApJ, 681, 925
Woo, J., & Urry, C. M. 2002, ApJ, 581, L5
Woo, J.-H., Urry, C. M., van der Marel, R. P., Lira, P., & Maza, J. 2005, ApJ, 631, 762
Wright, E. L. 2006, PASP, 118, 1711
Yu, Q., & Lu, Y. 2008, ApJ, 689, 732

TABLE 1

ID[a]	Optical Position RA	DEC	z	Rest-frame B (AB mag) Total	Pt src	Host	B/Tot	$\log M_{BH}$ ($M_\odot$)
N 48	188.983765	62.205441	0.940	21.741±0.012	···	21.74±0.01	$0.79^{+0.17}_{-0.30}$	$9.18^{+0.52}_{-0.51}$
N 72	189.023956	62.167603	0.936	22.020±0.007	23.40±0.19	22.38±0.23	$0.48^{+0.28}_{-0.26}$	$8.69^{+0.51}_{-0.50}$
N 76	189.027634	62.164326	0.637	21.389±0.010	26.79±0.39	21.40±0.21	$0.53^{+0.27}_{-0.27}$	$8.71^{+0.50}_{-0.50}$
N 82	189.033875	62.176731	0.681	20.990±0.004	22.90±0.24	21.19±0.24	$0.82^{+0.15}_{-0.30}$	$9.07^{+0.52}_{-0.52}$
N 90	189.046814	62.150940	1.140	22.340±0.013	24.48±0.14	22.50±0.20	$0.77^{+0.18}_{-0.29}$	$9.07^{+0.52}_{-0.52}$
N 93	189.050156	62.194221	0.275	19.784±0.001	23.08±0.21	19.84±0.23	$0.83^{+0.14}_{-0.30}$	$8.66^{+0.50}_{-0.50}$
N103	189.060364	62.121876	0.969	21.194±0.012	24.86±0.15	21.30±0.18	$0.39^{+0.29}_{-0.23}$	$9.08^{+0.52}_{-0.52}$
N110	189.070221	62.104027	1.141	21.479±0.008	26.23±0.26	21.48±0.19	$0.76^{+0.19}_{-0.29}$	$9.49^{+0.55}_{-0.55}$
N113	189.071228	62.169903	0.845	22.451±0.011	25.24±0.17	22.45±0.17	$0.87^{+0.12}_{-0.30}$	$8.81^{+0.50}_{-0.51}$
N116[b]	189.077530	62.187622	1.022	20.554±0.006	22.53±0.29	20.55±0.26	$0.32^{+0.33}_{-0.21}$	$9.36^{+0.54}_{-0.54}$
N127	189.088516	62.185921	1.014	21.881±0.011	26.22±0.26	21.88±0.19	$0.89^{+0.10}_{-0.30}$	$9.27^{+0.53}_{-0.53}$
N139	189.098541	62.310368	1.013	21.411±0.014	24.67±0.14	21.41±0.19	$0.75^{+0.19}_{-0.30}$	$9.39^{+0.54}_{-0.54}$
N150	189.114609	62.174030	0.762	23.115±0.023	26.69±0.38	23.11±0.19	$0.86^{+0.12}_{-0.30}$	$8.41^{+0.50}_{-0.49}$
N158	189.121506	62.179565	1.013	21.957±0.018	27.88±0.76	21.96±0.17	$0.13^{+0.30}_{-0.07}$	$8.35^{+0.49}_{-0.50}$
N160	189.122055	62.270576	0.848	21.464±0.005	24.00±0.14	21.46±0.22	$0.95^{+0.05}_{-0.30}$	$9.27^{+0.53}_{-0.53}$
N163	189.124893	62.095203	0.485	21.389±0.005	23.81±0.16	21.39±0.22	$0.69^{+0.22}_{-0.29}$	$8.53^{+0.50}_{-0.50}$
N164	189.125244	62.156734	0.953	22.425±0.009	25.23±0.16	22.42±0.17	$0.46^{+0.28}_{-0.26}$	$8.67^{+0.50}_{-0.50}$
N170	189.132751	62.295914	0.680	21.829±0.008	26.15±0.24	21.85±0.19	$0.05^{+0.22}_{-0.03}$	$7.50^{+0.52}_{-0.53}$
N174	189.138474	62.143036	0.934	21.084±0.005	22.52±0.30	21.42±0.26	$0.86^{+0.12}_{-0.30}$	$9.35^{+0.54}_{-0.54}$
N177	189.140244	62.168388	1.016	21.336±0.008	26.40±0.30	21.35±0.19	$0.39^{+0.29}_{-0.24}$	$9.12^{+0.52}_{-0.52}$
N187	189.145264	62.274620	0.847	22.444±0.015	25.77±0.19	22.50±0.18	$0.03^{+0.34}_{-0.03}$	$7.26^{+0.54}_{-0.54}$
N194	189.153198	62.199001	0.555	22.969±0.008	27.24±0.52	22.99±0.19	$0.73^{+0.20}_{-0.29}$	$8.04^{+0.50}_{-0.50}$
N201	189.160385	62.227596	1.020	22.059±0.015	25.84±0.19	22.09±0.18	$0.81^{+0.16}_{-0.30}$	$9.14^{+0.52}_{-0.52}$
N205	189.162918	62.162346	1.230	22.998±0.017	26.16±0.27	23.06±0.19	$1.00^{+0.00}_{-0.30}$	$9.04^{+0.51}_{-0.51}$
N217	189.173203	62.163483	0.518	21.497±0.005	28.74±1.08	21.50±0.17	$0.60^{+0.30}_{-0.35}$	$8.49^{+0.50}_{-0.50}$
N222	189.175827	62.262722	0.857	21.380±0.008	24.00±0.14	21.48±0.22	$0.66^{+0.24}_{-0.32}$	$9.11^{+0.52}_{-0.52}$
N240	189.193115	62.234734	0.961	20.867±0.005	22.85±0.24	21.06±0.24	$0.89^{+0.10}_{-0.30}$	$9.55^{+0.56}_{-0.55}$
N242	189.194107	62.149166	0.890	23.861±0.041	28.37±0.93	23.88±0.16	$0.49^{+0.30}_{-0.28}$	$8.01^{+0.50}_{-0.50}$
N261	189.209030	62.204823	0.902	21.971±0.010	26.91±0.43	21.98±0.20	$1.00^{+0.00}_{-0.30}$	$9.14^{+0.52}_{-0.52}$
N262	189.209595	62.334686	1.011	22.566±0.010	23.97±0.14	22.92±0.22	$0.47^{+0.28}_{-0.26}$	$8.54^{+0.50}_{-0.50}$
N266	189.213638	62.181107	1.100	22.975±0.017	25.89±0.19	23.05±0.18	$1.00^{+0.00}_{-0.30}$	$8.92^{+0.51}_{-0.51}$
N278	189.222992	62.338577	1.023	23.166±0.013	24.76±0.15	23.45±0.19	$0.56^{+0.27}_{-0.28}$	$8.40^{+0.49}_{-0.50}$
N286	189.231064	62.219883	0.955	21.626±0.008	24.52±0.14	21.70±0.19	$0.69^{+0.22}_{-0.29}$	$9.16^{+0.52}_{-0.52}$
N304	189.245163	62.243118	0.678	20.765±0.005	23.38±0.19	20.87±0.23	$0.56^{+0.26}_{-0.28}$	$9.02^{+0.52}_{-0.51}$
N309	189.249268	62.326241	1.144	22.582±0.017	24.92±0.14	22.72±0.18	$0.71^{+0.21}_{-0.30}$	$8.95^{+0.51}_{-0.51}$
N323[b]	189.261353	62.262199	0.514	20.393±0.002	21.72±0.41	20.77±0.54	$0.33^{+0.31}_{-0.21}$	$8.52^{+0.54}_{-0.54}$
N349	189.281601	62.332314	1.030	23.522±0.027	26.52±0.33	23.59±0.19	$1.00^{+0.00}_{-0.30}$	$8.62^{+0.50}_{-0.50}$
N352	189.282730	62.268341	0.936	20.980±0.006	26.69±0.37	20.99±0.20	$0.24^{+0.30}_{-0.16}$	$8.95^{+0.51}_{-0.51}$
N370	189.300629	62.298428	1.060	22.683±0.014	24.89±0.14	22.84±0.18	$0.92^{+0.08}_{-0.30}$	$8.93^{+0.51}_{-0.51}$
N373	189.307480	62.240242	0.475	22.628±0.006	28.17±0.85	22.63±0.16	$0.99^{+0.00}_{-0.30}$	$8.15^{+0.50}_{-0.50}$
N384	189.316345	62.203796	1.019	21.985±0.018	26.52±0.33	22.00±0.21	$0.31^{+0.30}_{-0.20}$	$8.74^{+0.50}_{-0.50}$
N390	189.319489	62.292667	1.146	22.123±0.008	22.98±0.22	22.78±0.23	$0.20^{+0.32}_{-0.13}$	$8.35^{+0.50}_{-0.50}$
N402	189.334732	62.231556	0.780	23.014±0.232	29.79±0.85	23.02±0.05	$0.02^{+0.20}_{-0.02}$	$6.83^{+0.58}_{-0.58}$
N405	189.340988	62.176670	0.978	21.181±0.006	25.00±0.14	21.18±0.17	$0.55^{+0.26}_{-0.27}$	$9.29^{+0.53}_{-0.53}$
N437	189.393890	62.232430	0.839	20.890±0.006	25.23±0.15	20.91±0.17	$0.27^{+0.30}_{-0.17}$	$8.91^{+0.51}_{-0.51}$
N442	189.402100	62.225620	0.852	22.193±0.009	24.76±0.14	22.30±0.18	$0.21^{+0.30}_{-0.14}$	$8.24^{+0.50}_{-0.50}$
N448	189.408051	62.219257	1.238	22.709±0.016	26.36±0.29	22.75±0.20	$0.36^{+0.29}_{-0.22}$	$8.71^{+0.50}_{-0.50}$
N451[b]	189.413559	62.349976	0.837	20.528±0.006	21.58±0.42	21.05±0.64	$0.01^{+0.19}_{-0.01}$	$7.17^{+0.60}_{-0.63}$
N471	189.462021	62.266979	1.170	21.007±0.006	24.12±0.14	21.07±0.21	$0.52^{+0.27}_{-0.27}$	$9.52^{+0.55}_{-0.55}$
N473[b]	189.469681	62.274593	0.307	19.467±0.001	20.67±0.47	19.90±1.12	$0.99^{+0.01}_{-0.30}$	$8.83^{+0.71}_{-0.68}$
S 44	53.015217	-27.767685	0.574	21.434±0.004	25.56±0.17	21.46±0.18	$0.71^{+0.21}_{-0.29}$	$8.70^{+0.50}_{-0.50}$
S 84	53.050934	-27.772406	1.033	21.866±0.010	25.50±0.17	21.91±0.18	$0.80^{+0.16}_{-0.30}$	$9.23^{+0.53}_{-0.52}$
S 88	53.055191	-27.711349	0.605	19.825±0.002	23.45±0.18	19.86±0.23	$0.90^{+0.09}_{-0.30}$	$9.54^{+0.56}_{-0.55}$
S 91	53.057728	-27.713583	0.735	21.240±0.006	25.68±0.18	21.26±0.18	$0.28^{+0.30}_{-0.18}$	$8.64^{+0.50}_{-0.50}$
S103[b]	53.062420	-27.857510	0.675	20.936±0.005	25.52±0.17	20.95±0.18	$0.27^{+0.30}_{-0.17}$	$8.65^{+0.50}_{-0.50}$
S117	53.071434	-27.717588	0.569	21.742±0.003	23.51±0.18	21.98±0.22	$0.31^{+0.29}_{-0.20}$	$8.09^{+0.50}_{-0.50}$
S118	53.071533	-27.872456	1.097	21.774±0.010	24.89±0.14	21.84±0.18	< 0.054	< 8.09
S134	53.085327	-27.792313	0.604	22.118±0.010	26.08±0.22	22.15±0.18	$0.53^{+0.27}_{-0.27}$	$8.33^{+0.49}_{-0.50}$

TABLE 1 — *Continued*

ID[a]	Optical Position RA	DEC	z	Rest-frame B (AB mag) Total	Pt src	Host	B/Tot	$\log M_{BH}$ ($M_\odot$)
S137	53.089264	-27.708660	0.736	21.587±0.007	24.64±0.14	21.65±0.19	$0.44^{+0.28}_{-0.25}$	$8.68^{+0.50}_{-0.50}$
S139	53.091618	-27.782206	0.668	20.893±0.006	24.49±0.14	20.93±0.20	$0.30^{+0.30}_{-0.19}$	$8.70^{+0.50}_{-0.50}$
S151	53.096489	-27.765188	1.223	22.328±0.016	25.25±0.16	22.40±0.17	< 0.055	< 8.00
S155	53.101063	-27.690676	0.534	21.707±0.006	24.98±0.14	21.76±0.17	$0.76^{+0.19}_{-0.30}$	$8.52^{+0.50}_{-0.50}$
S156	53.102264	-27.669563	0.890	22.545±0.011	27.73±0.70	22.55±0.17	$0.84^{+0.13}_{-0.30}$	$8.81^{+0.50}_{-0.50}$
S159	53.103516	-27.933329	1.170	23.112±0.027	26.83±0.40	23.15±0.22	$0.89^{+0.10}_{-0.30}$	$8.90^{+0.51}_{-0.51}$
S160	53.103989	-27.835567	1.037	23.945±0.033	25.94±0.20	24.13±0.28	$0.45^{+0.32}_{-0.27}$	$8.03^{+0.51}_{-0.51}$
S161	53.104088	-27.683752	0.733	21.446±0.005	24.19±0.14	21.54±0.21	$0.81^{+0.16}_{-0.30}$	$9.00^{+0.52}_{-0.51}$
S162	53.104607	-27.845348	1.043	22.646±0.013	24.97±0.14	22.78±0.31	$0.99^{+0.01}_{-0.30}$	$8.97^{+0.52}_{-0.52}$
S164	53.104836	-27.913925	1.090	21.209±0.005	24.88±0.14	21.25±0.18	$0.52^{+0.27}_{-0.27}$	$9.37^{+0.53}_{-0.54}$
S171	53.107746	-27.918444	1.034	22.623±0.019	26.37±0.29	22.66±0.20	< 0.056	< 7.71
S176	53.111511	-27.695988	0.734	21.887±0.009	24.39±0.14	22.00±0.20	$0.35^{+0.29}_{-0.22}$	$8.42^{+0.49}_{-0.49}$
S179[b]	53.115097	-27.695805	0.668	21.614±0.005	24.83±0.14	21.67±0.18	$0.62^{+0.25}_{-0.28}$	$8.72^{+0.50}_{-0.50}$
S184	53.120827	-27.958441	0.640	20.284±0.004	21.78±0.40	20.60±0.48	$0.40^{+0.29}_{-0.24}$	$8.92^{+0.55}_{-0.54}$
S193[b]	53.125252	-27.756536	0.960	21.793±0.009	23.02±0.22	22.22±0.23	< 0.055	< 7.79
S200	53.133675	-27.698660	0.960	23.000±0.028	24.56±0.14	23.30±0.19	$0.21^{+0.33}_{-0.14}$	$7.95^{+0.50}_{-0.51}$
S203	53.137436	-27.688057	1.050	20.922±0.007	25.13±0.15	20.94±0.17	$0.98^{+0.02}_{-0.30}$	$9.74^{+0.57}_{-0.57}$
S214	53.145634	-27.919777	0.839	22.182±0.010	24.42±0.14	22.33±0.20	$0.65^{+0.24}_{-0.29}$	$8.72^{+0.51}_{-0.50}$
S220	53.149342	-27.683189	0.735	21.764±0.006	25.82±0.19	21.79±0.18	$0.50^{+0.27}_{-0.27}$	$8.68^{+0.50}_{-0.50}$
S227	53.152973	-27.735123	0.665	22.059±0.010	24.28±0.14	22.21±0.21	$0.89^{+0.09}_{-0.30}$	$8.65^{+0.51}_{-0.50}$
S229	53.156075	-27.666695	0.664	22.164±0.008	23.03±0.22	22.81±0.23	$0.13^{+0.30}_{-0.07}$	$7.51^{+0.52}_{-0.53}$
S249	53.173805	-27.724491	0.979	22.637±0.017	27.09±0.48	22.66±0.20	$0.45^{+0.30}_{-0.26}$	$8.59^{+0.50}_{-0.50}$
S263[b]	53.185226	-27.827835	1.016	22.308±0.008	24.25±0.14	22.51±0.21	$0.69^{+0.22}_{-0.29}$	$8.89^{+0.51}_{-0.51}$
S271	53.195938	-27.729589	1.178	22.146±0.022	25.17±0.15	22.22±0.18	$0.51^{+0.27}_{-0.27}$	$9.04^{+0.52}_{-0.51}$
S273	53.196571	-27.863205	1.069	22.252±0.009	24.70±0.14	22.37±0.19	$0.29^{+0.29}_{-0.18}$	$8.60^{+0.50}_{-0.50}$
S276	53.200741	-27.882389	0.667	20.303±0.004	23.04±0.22	20.39±0.23	$0.48^{+0.28}_{-0.26}$	$9.14^{+0.53}_{-0.52}$
S286[b]	53.220360	-27.855505	1.227	21.830±0.009	23.22±0.20	22.18±0.23	$0.03^{+0.21}_{-0.03}$	$7.85^{+0.51}_{-0.51}$
S293	53.237385	-27.835745	1.143	21.909±0.009	26.02±0.21	21.93±0.19	$0.86^{+0.12}_{-0.30}$	$9.36^{+0.54}_{-0.53}$
S300	53.245888	-27.861118	1.010	23.964±0.047	26.99±0.45	24.03±0.20	$0.28^{+0.36}_{-0.19}$	$7.83^{+0.51}_{-0.51}$

[a] X-ray IDs from Alexander et al. (2003)
[b] Broad-Line AGN (Cowie et al. 2003; Wirth et al. 2004; Szokoly et al. 2004).

TABLE 2
Bolometric luminosities derived from reddened SEDs[a], L_X correction[b], direct integration[c], and comparison model[d].

ID	$\log L_X$[e]	$\log N_H$[f]	$E(B-V)$	N_{pt}	$\log L_{bol}$[a, e]	$\log L_{bol,X}$[b, e]	$\log L_{\rm tot,obs}$[c, e]	$\log L_{bol,\rm T09}$[d, e]	$\log \lambda_{edd}$[g]
N 48	44.08	23.30	$1.10^{+0.04}_{-0.15}$	2	45.25	45.24	45.25	45.90	$-2.04^{+0.52}_{-0.52}$
N 72	42.83	22.85	$0.01^{+0.09}_{-0.00}$	2	45.19	43.99	45.02	44.40	$-1.68^{+0.54}_{-0.55}$
N 76	44.21	23.98	$0.82^{+0.17}_{-0.12}$	3	44.95	45.36	45.05	46.05	$-1.87^{+0.50}_{-0.50}$
N 82	42.61	22.69	$0.13^{+0.11}_{-0.12}$	3	45.07	43.77	45.25	44.14	$-2.20^{+0.54}_{-0.56}$
N 90	43.54	23.09	$0.27^{+0.30}_{-0.25}$	1	45.28	44.70	45.34	45.25	$-2.00^{+0.54}_{-0.56}$
N 93	42.60	21.32	$0.42^{+0.04}_{-0.05}$	4	44.09	43.76	44.72	44.13	$-2.67^{+0.50}_{-0.50}$
N103	42.54	20.27	$0.43^{+0.30}_{-0.42}$	3	44.69	43.70	45.26	44.06	$-2.50^{+0.52}_{-0.52}$
N110	42.77	20.81	$0.29^{+0.30}_{-0.28}$	2	44.74	43.93	45.32	44.33	$-2.97^{+0.57}_{-0.59}$
N113	43.15	21.32	$0.51^{+0.11}_{-0.17}$	3	44.58	44.31	45.02	44.79	$-2.33^{+0.51}_{-0.50}$
N116[h]	43.92	20.29	$0.05^{+0.10}_{-0.02}$	4	45.35	45.07	45.60	45.70	$-2.11^{+0.55}_{-0.55}$
N127	43.52	23.52	$0.74^{+0.29}_{-0.13}$	2	45.09	44.68	45.24	45.23	$-2.30^{+0.53}_{-0.53}$
N139	43.00	21.04	$0.26^{+0.30}_{-0.25}$	2	44.70	44.16	45.25	44.60	$-2.83^{+0.54}_{-0.54}$
N150	42.97	22.93	$0.61^{+0.18}_{-0.13}$	2	44.34	44.12	44.40	44.56	$-2.19^{+0.50}_{-0.50}$
N158	43.09	22.91	$1.45^{+0.05}_{-1.17}$	2	45.05	44.25	45.37	44.72	$-1.43^{+0.50}_{-0.50}$
N160	43.10	23.08	$0.36^{+0.15}_{-0.12}$	4	44.83	44.25	45.25	44.72	$-2.57^{+0.53}_{-0.54}$
N163	43.62	23.90	$0.31^{+0.30}_{-0.30}$	3	45.02	44.78	45.00	45.34	$-2.03^{+0.64}_{-1.09}$
N164	44.49	23.61	$0.47^{+0.14}_{-0.11}$	4	45.11	45.65	44.99	46.39	$-1.67^{+0.50}_{-0.50}$
N170	42.50	22.43	$0.54^{+0.03}_{-0.03}$	3	44.44	43.66	44.76	44.01	$-1.16^{+0.53}_{-0.52}$
N174	43.40	19.32	$0.01^{+0.04}_{-0.00}$	2	45.09	44.56	45.43	45.08	$-2.32^{+0.54}_{-0.55}$
N177	42.59	21.74	$0.38^{+0.01}_{-0.37}$	3	44.86	43.75	45.31	44.12	$-2.40^{+0.52}_{-0.53}$

TABLE 2 — *Continued*

ID	$\log L_X$[e]	$\log N_H$[f]	$E(B-V)$	N_{pt}	$\log L_{bol}$[a, e]	$\log L_{bol,X}$[b, e]	$\log L_{\rm tot,obs}$[c, e]	$\log L_{bol,\rm T09}$[d, e]	$\log \lambda_{edd}$[g]
N187	42.56	23.27	$0.61^{+0.02}_{-0.60}$	4	44.74	43.72	44.99	44.08	$-0.58^{+0.55}_{-0.54}$
N194	42.63	19.95	$0.62^{+0.30}_{-0.08}$	4	43.89	43.79	44.37	44.17	$-2.26^{+0.50}_{-0.50}$
N201	43.10	23.69	$1.02^{+0.03}_{-1.01}$	2	44.71	44.26	44.79	44.73	$-2.48^{+0.52}_{-0.53}$
N205	43.29	21.69	$0.34^{+0.05}_{-0.06}$	4	44.92	44.45	45.04	44.96	$-2.23^{+0.51}_{-0.51}$
N217	42.79	23.70	$1.60^{+0.05}_{-1.59}$	4	44.57	43.94	45.00	44.35	$-1.97^{+0.51}_{-0.50}$
N222	42.79	21.35	$0.25^{+0.30}_{-0.24}$	3	44.95	43.95	45.36	44.35	$-2.28^{+0.52}_{-0.52}$
N240	44.07	22.63	$0.99^{+0.11}_{-0.22}$	2	45.22	45.23	45.41	45.89	$-2.43^{+0.55}_{-0.56}$
N242	42.66	23.42	$5.00^{+0.16}_{-0.16}$	4	44.29	43.82	44.50	44.20	$-1.82^{+0.50}_{-0.50}$
N261	42.55	23.49	$0.52^{+0.02}_{-0.51}$	4	44.58	43.71	44.80	44.06	$-2.59^{+0.53}_{-0.53}$
N262	42.90	20.18	$1.79^{+0.06}_{-1.77}$	1	44.21	44.06	44.74	44.49	$-2.43^{+0.50}_{-0.50}$
N266	43.49	23.61	$0.62^{+0.08}_{-0.06}$	4	44.95	44.65	44.90	45.19	$-2.08^{+0.51}_{-0.51}$
N278	43.00	23.29	$0.80^{+0.30}_{-0.14}$	1	44.72	44.16	44.72	44.60	$-1.81^{+0.50}_{-0.50}$
N286	42.73	21.68	$1.31^{+0.04}_{-1.30}$	2	44.34	43.89	45.10	44.28	$-2.91^{+0.52}_{-0.52}$
N304	43.20	20.94	$0.17^{+0.15}_{-0.07}$	3	44.62	44.35	45.07	44.84	$-2.57^{+0.52}_{-0.53}$
N309	43.04	21.30	$0.88^{+0.30}_{-0.54}$	1	44.59	44.20	45.04	44.66	$-2.46^{+0.51}_{-0.51}$
N323[h]	43.50	21.97	$0.19^{+0.16}_{-0.09}$	4	44.90	44.66	45.18	45.21	$-1.79^{+0.55}_{-0.55}$
N349	42.94	21.84	$0.55^{+0.02}_{-0.01}$	4	44.44	44.09	44.61	44.53	$-2.24^{+0.50}_{-0.50}$
N352	42.73	23.13	$5.00^{+0.00}_{-0.16}$	3	44.70	43.89	45.29	44.28	$-2.39^{+0.51}_{-0.52}$
N370	43.01	20.96	$0.30^{+0.08}_{-0.07}$	4	44.65	44.17	44.95	44.62	$-2.38^{+0.51}_{-0.51}$
N373	42.63	22.77	$1.52^{+0.05}_{-1.51}$	4	44.11	43.79	44.36	44.16	$-2.09^{+0.51}_{-0.50}$
N384	43.64	23.39	$2.38^{+0.08}_{-1.63}$	2	44.93	44.80	45.15	45.37	$-1.90^{+0.50}_{-0.50}$
N390	44.13	22.35	$1.39^{+0.05}_{-1.37}$	1	45.66	45.29	45.59	45.96	$-0.82^{+0.50}_{-0.51}$
N402	42.81	23.20	$1.24^{+0.17}_{-0.18}$	4	44.47	43.97	44.64	44.37	$-0.46^{+0.59}_{-0.58}$
N405	43.24	23.41	$1.40^{+0.05}_{-1.34}$	3	44.83	44.40	45.25	44.89	$-2.54^{+0.53}_{-0.53}$
N437	42.83	21.36	$0.58^{+0.03}_{-0.11}$	4	44.62	43.99	45.31	44.40	$-2.40^{+0.51}_{-0.51}$
N442	43.16	23.89	$0.13^{+0.04}_{-0.02}$	4	44.97	44.32	44.85	44.79	$-1.41^{+0.50}_{-0.51}$
N448	43.47	23.16	$1.39^{+0.05}_{-0.97}$	1	44.89	44.62	45.09	45.16	$-1.91^{+0.50}_{-0.50}$
N451[h]	43.96	21.06	$0.01^{+0.30}_{-0.00}$	3	45.53	45.11	45.53	45.75	$0.29^{+0.63}_{-0.60}$
N471	42.84	22.90	$0.96^{+0.19}_{-0.16}$	3	44.90	44.00	45.58	44.41	$-2.73^{+0.55}_{-0.55}$
N473[h]	43.28	18.23	$0.13^{+0.01}_{-0.00}$	3	44.60	44.44	45.05	44.94	$-2.33^{+0.69}_{-0.71}$
S 44	43.38	22.87	$0.77^{+0.10}_{-0.11}$	3	44.69	44.54	45.00	45.06	$-2.11^{+0.50}_{-0.50}$
S 84	42.72	22.42	$0.98^{+0.13}_{-0.21}$	2	44.72	43.87	45.06	44.26	$-2.61^{+0.53}_{-0.53}$
S 88	43.49	22.42	$0.50^{+0.01}_{-0.00}$	4	44.94	44.65	45.21	45.19	$-2.70^{+0.56}_{-0.56}$
S 91	43.08	23.57	$0.68^{+0.17}_{-0.22}$	3	44.72	44.24	44.96	44.70	$-2.02^{+0.50}_{-0.50}$
S103[h]	42.90	19.98	$0.95^{+0.03}_{-0.94}$	2	44.35	44.06	44.92	44.48	$-2.40^{+0.50}_{-0.50}$
S117	43.12	20.46	$0.01^{+0.00}_{-0.01}$	3	44.58	44.28	44.78	44.75	$-1.60^{+0.50}_{-0.50}$
S118	44.23	23.30	$1.31^{+0.30}_{-1.30}$	2	45.26	45.39	45.26	46.08	> -0.93
S134	43.33	23.26	$0.96^{+0.26}_{-0.16}$	2	44.52	44.48	44.47	44.99	$-1.93^{+0.50}_{-0.50}$
S137	42.92	23.38	$0.44^{+0.14}_{-0.15}$	3	44.63	44.08	44.80	44.51	$-2.17^{+0.51}_{-0.51}$
S139	42.84	23.71	$0.10^{+0.30}_{-0.09}$	4	44.96	43.99	44.98	44.41	$-1.84^{+0.54}_{-0.54}$
S151	42.50	21.76	$1.25^{+0.30}_{-0.98}$	2	44.53	43.66	44.99	44.01	> -1.56
S155	42.73	21.22	$0.41^{+0.09}_{-0.11}$	3	44.16	43.89	44.76	44.28	$-2.46^{+0.50}_{-0.50}$
S156	43.28	22.65	$0.43^{+0.30}_{-0.29}$	4	44.72	44.43	44.91	44.94	$-2.25^{+0.51}_{-0.52}$
S159	43.57	21.76	$1.22^{+0.04}_{-1.10}$	1	44.63	44.73	44.75	45.29	$-2.36^{+0.51}_{-0.51}$
S160	43.02	23.19	$0.28^{+0.30}_{-0.20}$	4	44.58	44.18	44.16	44.63	$-1.90^{+0.64}_{-0.97}$
S161	43.19	22.86	$0.47^{+0.05}_{-0.07}$	3	44.69	44.35	44.84	44.83	$-2.40^{+0.51}_{-0.52}$
S162	42.69	22.69	$0.22^{+0.01}_{-0.21}$	4	44.55	43.85	44.49	44.24	$-2.47^{+0.53}_{-0.53}$
S164	43.53	23.56	$1.03^{+0.03}_{-1.02}$	2	45.04	44.69	45.29	45.24	$-2.42^{+0.54}_{-0.54}$
S171	42.55	21.32	$0.53^{+0.02}_{-0.02}$	2	44.44	43.71	44.78	44.06	> -1.41
S176	43.01	22.35	$0.01^{+0.30}_{-0.00}$	3	45.01	44.16	44.87	44.61	$-1.58^{+0.52}_{-0.54}$
S179[h]	43.38	22.85	$0.90^{+0.03}_{-0.89}$	2	44.87	44.54	44.82	45.06	$-1.93^{+0.50}_{-0.50}$
S184	42.86	21.16	$0.01^{+0.00}_{-0.01}$	3	44.74	44.02	45.16	44.44	$-2.26^{+0.54}_{-0.55}$
S193[h]	43.29	21.05	$0.53^{+0.30}_{-0.18}$	2	44.90	44.45	45.18	44.95	> -1.00
S200	42.92	21.91	$0.35^{+0.01}_{-0.02}$	4	44.77	44.08	44.83	44.51	$-1.32^{+0.51}_{-0.51}$
S203	42.75	22.81	$0.44^{+0.06}_{-0.10}$	4	44.83	43.90	45.35	44.30	$-3.01^{+0.57}_{-0.57}$
S214	43.16	21.70	$0.42^{+0.03}_{-0.07}$	3	44.68	44.32	44.81	44.80	$-2.14^{+0.50}_{-0.51}$
S220	43.21	23.23	$0.64^{+0.06}_{-0.06}$	3	44.56	44.37	44.71	44.86	$-2.22^{+0.50}_{-0.50}$
S227	43.32	21.46	$0.49^{+0.01}_{-0.01}$	2	44.38	44.47	44.52	44.98	$-2.33^{+0.50}_{-0.51}$
S229	42.98	20.07	$0.06^{+0.03}_{-0.01}$	2	44.36	44.14	44.53	44.58	$-1.26^{+0.53}_{-0.52}$

TABLE 2 — *Continued*

ID	$\log L_X$ [e]	$\log N_H$ [f]	$E(B-V)$	N_{pt}	$\log L_{bol}$ [a, e]	$\log L_{bol,X}$ [b, e]	$\log L_{\rm tot,obs}$ [c, e]	$\log L_{bol,\rm T09}$ [d, e]	$\log \lambda_{edd}$ [g]
S249	43.36	23.74	$0.47^{+0.12}_{-0.15}$	4	44.89	44.52	44.88	45.04	$-1.80^{+0.50}_{-0.50}$
S263[h]	43.47	22.77	$5.00^{+0.16}_{-0.16}$	1	44.31	44.63	44.70	45.17	$-2.67^{+0.51}_{-0.51}$
S271	43.29	23.11	$0.54^{+0.30}_{-0.53}$	2	44.97	44.45	45.04	44.96	$-2.19^{+0.52}_{-0.52}$
S273	42.41	21.37	$0.20^{+0.30}_{-0.16}$	2	44.33	43.57	44.79	43.90	$-2.39^{+0.50}_{-0.50}$
S276	42.65	22.65	$0.01^{+0.10}_{-0.00}$	3	44.97	43.81	45.13	44.19	$-2.40^{+0.57}_{-0.62}$
S286[h]	43.74	20.85	$0.30^{+0.30}_{-0.20}$	2	45.27	44.89	45.29	45.48	$-0.68^{+0.51}_{-0.51}$
S293	42.56	19.49	$5.00^{+0.00}_{-0.16}$	2	44.28	43.71	45.06	44.07	$-3.18^{+0.54}_{-0.55}$
S300	42.74	21.50	$0.66^{+0.30}_{-0.65}$	4	44.56	43.90	44.68	44.30	$-1.38^{+0.51}_{-0.51}$

[a] Method 1 in Section 4.3; described in detail in Section 4.2.
[b] Method 2 in Section 4.3; described in detail in Section 4.1.
[c] Method 3 in Section 4.3.
[d] Method 4 in Section 4.3; from Treister et al. (2009).
[e] All luminosities are in *cgs* (erg s^{-1}).
[f] Gas column density in cm^{-2}.
[g] Calculated using L_{bol} from Method 1.
[h] Broad-Line AGN (Cowie et al. 2003; Wirth et al. 2004; Szokoly et al. 2004).